

1 **Spatial variation in shallow slow earthquake activity in Hyuga-nada, southwest Japan**

2
3 Satoru Baba^{1,2}, Shunsuke Takemura¹, Kazushige Obara¹, Akiko Takeo¹, Yusuke Yamashita³, and
4 Masanao Shinohara¹

5
6 1. Earthquake Research Institute, the University of Tokyo, 1-1-1, Yayoi, Bunkyo-ku, Tokyo, 113-
7 0032, Japan

8 2. Now at Japan Agency for Marine-Earth Science and Technology, 2-15, Natsushima-cho,
9 Yokosuka, Kanagawa, 237-0061, Japan

10 3. Miyazaki Observatory, Disaster Prevention Research Institute, Kyoto University, 3884 Kaeda,
11 Miyazaki, Miyazaki, 889-2161, Japan

12
13 **Abbreviated title:** Spatial variation in slow earthquakes in Hyuga-nada

14
15 **Corresponding author:** Satoru Baba

16 E-mail: babasatoru@jamstec.go.jp

17 Phone: +81-46-867-9342

20 **Summary**

21 Hyuga-nada, off the Pacific coast of Kyushu along the Nankai Trough in southwest Japan,
22 is one of the most active slow earthquake regions around Japan. We estimated the energies of shallow
23 tremors and moments of shallow very low frequency earthquakes (VLFs) in Hyuga-nada using data
24 from a permanent onshore broadband network and temporary ocean bottom seismometer observations.
25 The energies and moments of these slow earthquakes have a similar along-strike variation and are
26 generally larger south of the subducted Kyushu-Palau Ridge than near the top of the ridge. This spatial
27 variation is also related to the characteristics of slow earthquake migration. The along-strike migration
28 speed was faster at initiation in the south, where the moments of slow earthquakes are larger. After
29 migration entered the subducted Kyushu-Palau Ridge, its speed is decelerated with a parabolic pattern
30 and their moments became smaller. Assuming a constant patch size of slow earthquakes, we estimated
31 that the stress drop of VLFs in the south of the subducted ridge was approximately three times larger
32 than that near the top of the subducted ridge. This stress drop difference between adjacent regions may
33 cause parabolic migration. According to our observations and physical models, the stress drops of
34 VLFs in the south and near the top of the subducted ridge may be higher and lower, respectively. We
35 also estimated the scaled energy of slow earthquakes from the ratio of the seismic energy rates of
36 tremors to the seismic moment rates of accompanying VLFs. The dominant range of scaled energy
37 of slow earthquakes in Hyuga-nada is 10^{-11} – 10^{-8} . In addition to having similar or one order smaller
38 values compared to other slow earthquake regions, the range of scaled energy in Hyuga-nada is broader.
39 This broader range suggests wide range of characteristic time and various spectral features of slow
40 earthquakes in Hyuga-nada. Based on a Brownian slow earthquake model, the wide range of
41 characteristic time in this area suggests width variations of slow earthquake source area.

42

43 **Keywords:** Subduction zone processes, Seismicity and tectonics, Earthquake source observations,
44 Japan

45

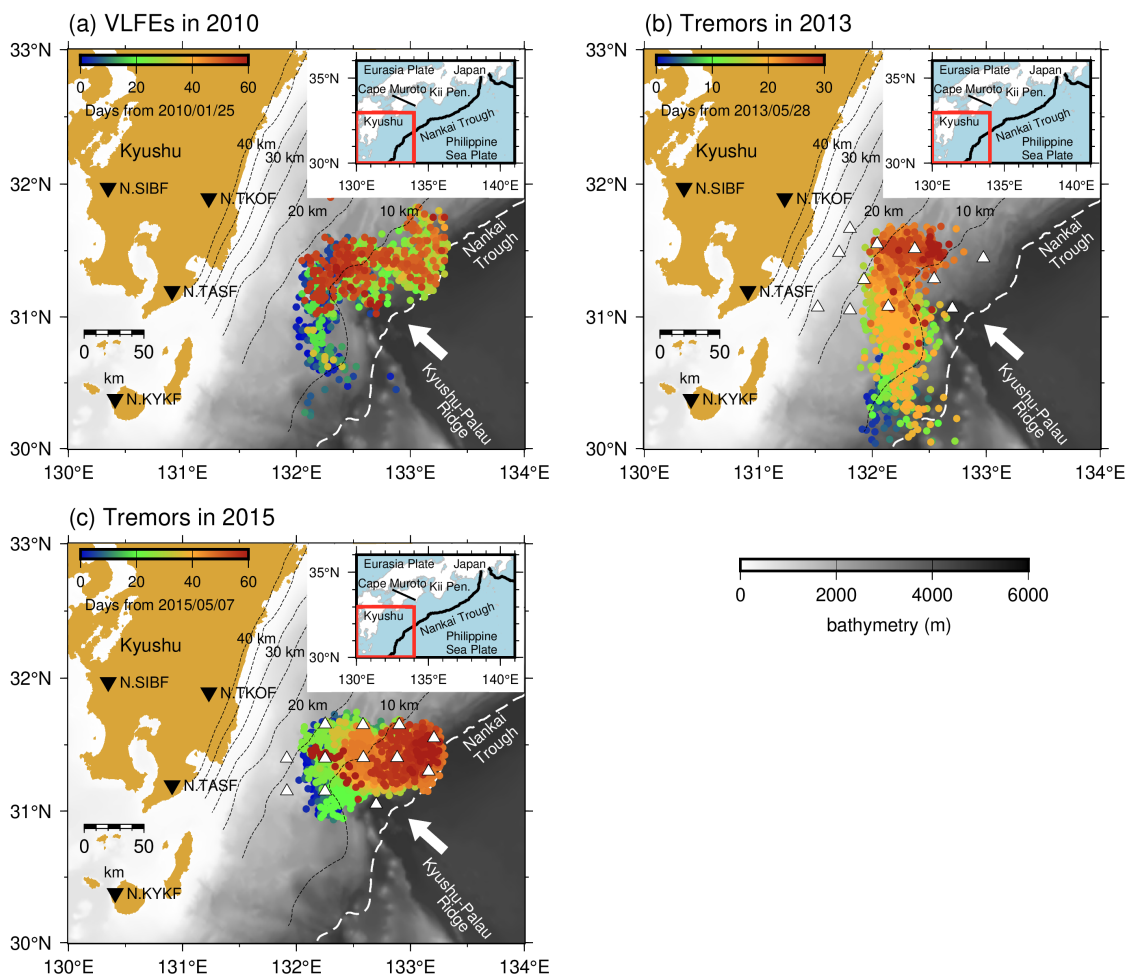
46

47 **1. Introduction**

48 After the discovery of tectonic low frequency tremors by Obara (2002), slow earthquakes,
49 which are fault slips with longer characteristic durations than regular earthquakes with the same
50 seismic moment (Ide *et al.* 2007), were mainly detected around seismogenic zones on plate boundaries
51 of subduction zones in the world. Seismic slow earthquakes are classified into tremors and low
52 frequency earthquakes (e.g., Shelly *et al.* 2006) observed in a frequency range of 2–8 Hz, and very
53 low frequency earthquakes (VLFs) observed in a frequency range of 0.02–0.05 Hz (e.g., Obara &
54 Ito 2005). Slow slip events (SSEs) are geodetically observed as crustal deformations, with duration
55 ranging from several days to several years (e.g., Dragert *et al.* 2001; Hirose *et al.* 1999). The
56 spatiotemporal correlation of these slow earthquake phenomena is known as episodic tremor and slip
57 (ETS; Rogers & Dragert 2003). The focal mechanisms of slow earthquakes in subduction zones are
58 thrust-type and consistent with those of megathrust earthquakes along plate boundaries. In addition,
59 slow earthquake activity can reflect the stress conditions on the plate boundary around the slow
60 earthquake regions (e.g., Obara & Kato 2016). Recent studies have revealed that slow earthquakes can
61 potentially trigger megathrust earthquakes (e.g., Kato *et al.* 2012; Vaca *et al.* 2018). Thus, studies of
62 slow earthquakes are important for understanding the slip behaviours on the plate boundary and the
63 occurrence mechanism of megathrust earthquakes.

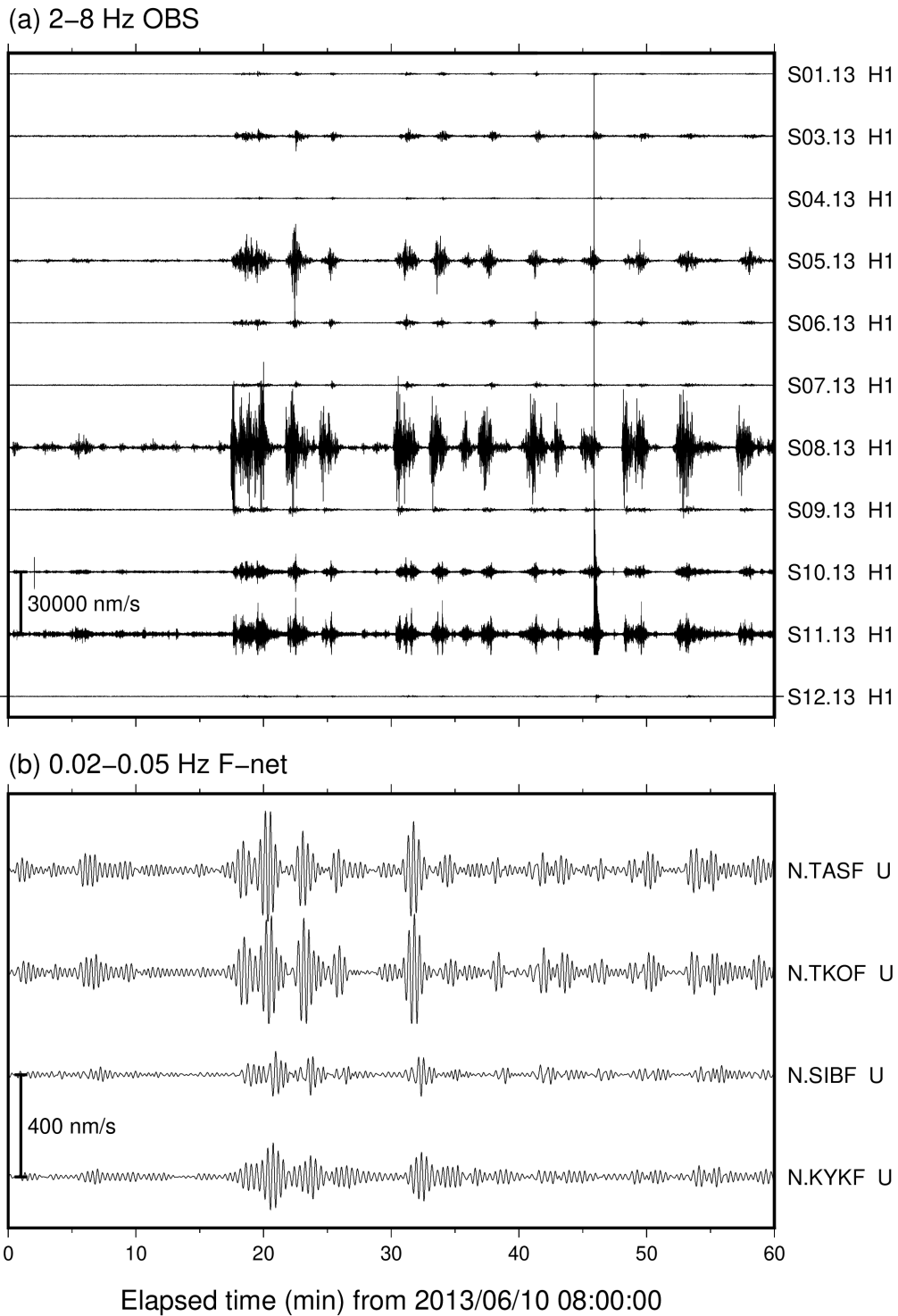
64 Around the Japanese islands, slow earthquakes occur in shallower and deeper extensions of
65 the seismogenic zone in southwest Japan along the Nankai Trough and in the offshore region of
66 northeastern Japan along the Japan Trench. In Hyuga-nada, off the Pacific coast of Kyushu, VLFs
67 are the most active around Japan (Baba *et al.* 2020). In this area, Asano *et al.* (2015) reported the
68 migration of shallow VLFs, which can be considered as a proxy for rupture propagation of an SSE
69 (e.g., Bartlow *et al.* 2011; Ito *et al.* 2007), in 2010 (Fig. 1a). VLFs first migrated from 30.5° N to
70 31.5° N along the strike direction and changed to along-dip migration at the subducted Kyushu-Palau
71 Ridge, which is subducting from the Nankai Trough. Although VLFs are observed by onshore
72 stations owing to the effective propagation of surface waves along shallower low velocity structures,
73 it is difficult to identify weak signals of shallow tremors in Hyuga-nada using permanent onshore
74 stations. Yamashita *et al.* (2015) and Yamashita *et al.* (2021) detected shallow tremors and reported
75 their migrations in Hyuga-nada utilizing temporary ocean bottom seismometers (OBSs) in 2013 and
76 2015, respectively (Fig. 1b and c). In 2013, tremors migrated twice from 30.3° N to 31.7° N. In 2015,
77 tremors migrated from west to east, north of 31° N and extended near the trench axis (Yamashita *et al.*
78 2021). The shallow tremors in Hyuga-nada were temporally correlated with shallow VLFs (Fig. 2).
79 The spatial distributions of tremors in both 2013 and 2015 were contained by those of VLFs in 2010.
80 Temporary OBS observations also revealed a high-resolution distribution of VLFs. Tonegawa *et al.*
81 (2020) suggested that the depths of shallow VLFs near the subducted Kyushu-Palau Ridge are
82 approximately 5 km different from the surrounding area.

83 The tectonic regime in Hyuga-nada is very characteristic; the Kyushu-Palau Ridge is
 84 subducted and the trench axis bends around the subduction of the ridge (Fig. 1). In addition, repeating
 85 earthquakes representing quasi-static slips on the plate boundary (e.g., Nadeau & McEvelly 1999;
 86 Uchida et al. 2003) occur in the downdip of shallow slow earthquakes (e.g., Igarashi, 2020; Yamashita
 87 et al., 2012). Tectonic conditions can affect the source process, such as the moment rate, of slow
 88 earthquakes (Baba et al. 2020; Takemura et al. 2022b). To investigate the spatial relationships between
 89 slow earthquake activity and tectonic conditions in Hyuga-nada, we quantitatively estimated the
 90 spatial variation in the source characteristics of slow earthquakes, such as the energy rate functions of
 91 tremors and the moment rate functions of VLFs, at high spatial resolution using onshore and offshore
 92 data.
 93



94
 95
 96 **Figure 1.** Slow earthquake activity in Hyuga-nada. Coloured dots are epicentres of (a) shallow VLFs
 97 in 2010 detected by Asano et al. (2015), (b) shallow tremors in 2013 detected by Yamashita et al.
 98 (2015), and (c) shallow tremors in 2015 detected by Yamashita et al. (2021). The colours of dots

99 correspond to days from the first activity for each tremor. White triangles represent the locations of
100 the OBSs utilized in the shallow tremor analysis. Inverted triangles exhibit the locations of the F-net
101 stations utilized in the shallow VLFE analysis. White arrows indicate the direction of the motion of
102 the Philippine Sea Plate relative to the Eurasia Plate (NUVEL-1A; DeMets et al., 1994). White dashed
103 lines represent the trench axis. Background grey scale denotes the bathymetry (ETOPO1; Amante &
104 Eakins 2009). Dashed contours indicate the isodepth at the top of the Philippine Sea plate in intervals
105 of 5 km (Nakanishi *et al.* 2018). Black lines in the inset represent the boundaries between the plates.
106



107

108

109 **Figure 2.** Example of one-hour records for (a) shallow tremors in a frequency range of 2–8 Hz at

110 OBSs and (b) shallow VLFES in a frequency range of 0.02–0.05 Hz at F-net stations.

111

112 **2. Data and Method**

113 **2.1. Estimation of energy rate functions of tremors**

114 For the analysis of tremors, we evaluated the energy rate functions of tremors located by
 115 Yamashita et al. (2015; 2021). We used 360 s broadband (NK1508 and NK1510 in 2015), 1 Hz (S06.13,
 116 S09.13 in 2013 and others in 2015) and 4.5 Hz (others in 2013) short-period OBS records of temporary
 117 seismological observations in Hyuga-nada. 11 and 12 stations were incorporated from April 17 to July
 118 4, 2013 (Yamashita et al. 2015) and from January 1, 2015 to January 1, 2016 (Yamashita et al. 2021),
 119 respectively. The sampling rate was 200 Hz (S05.13, S06.13, S08.13, and S09.13 in 2013 and all OBSs
 120 in 2015) or 128 Hz (other OBSs in 2013). Analog seismic signals were digitized using a 16-, 20-, or
 121 24-bit A/D converter. After instrumental responses were removed, a bandpass filter was applied in a
 122 frequency range of 2–8 Hz, and the vertical and horizontal components of the root-mean-square
 123 (RMS) velocity envelopes with a smoothing time window of 5 s were calculated. The envelopes were
 124 resampled at one sample per second. Examples of envelope waveforms of a tremor obtained by the
 125 RMS of the sums squared seismograms of two horizontal components are displayed in Fig. 3.

126 We estimated the site amplification factors of the vertical and horizontal components at
 127 each OBS relative to an F-net (Aoi *et al.* 2020) station, N.TASF, at 2–8 Hz and the quality factor of
 128 the *S*-wave attenuation (*Q*) by utilizing the information of the maximum *S*-wave amplitudes of
 129 intraslab regular earthquakes following the method of Yabe et al. (2019). The maximum *S*-wave
 130 amplitude of the *i*-th earthquake at the *j*-th station (A_{ij}) is expressed by the following relationship:

131
$$\ln(A_{ij}) = \ln(S_i) - \ln(\sqrt{4\pi}L_{ij}) - \frac{\pi f_c Q^{-1}}{V_s} L_{ij} + \ln(C_j) \quad (1)$$

132 where S_i is the size of the *i*-th seismic source, L_{ij} is the distance between the hypocentre of the *i*-th
 133 earthquake and the *j*-th station, f_c represents the central frequency (5 Hz in this study), V_s is the *S*-wave
 134 velocity (assuming 3.5 km/s in this study), and C_j is the site amplification factor. We measured the
 135 maximum *S*-wave amplitudes of regular earthquakes more than 5 km deeper than the plate boundary
 136 of the Japan Integrated Velocity Structure Model (JIVSM; Koketsu et al. 2012) with magnitudes larger
 137 than 2.5 listed in the regular earthquake catalogue of the Japan Meteorological Agency (Fig. S1). We
 138 defined the maximum envelope amplitude of the time window from 2 s before to 50 s after the arrival
 139 time at each OBS as the maximum *S*-wave amplitude. The site amplification factor relative to N.TASF
 140 and Q^{-1} at each OBS was estimated by solving Equation (1) using the least-squares method. In the
 141 following procedures, we utilized the RMS of the sums of the squared three-component seismograms
 142 with a smoothing time window of 5 s after site correction by implementing the site amplification
 143 factors displayed in Fig. 4. After correcting the site amplification factors, the amplitudes were
 144 normalized by the site conditions at the reference onshore station, N.TASF. We also evaluated the
 145 average of Q^{-1} solved at each OBS in Equation (1) as $(3.4415 \pm 0.9585) \times 10^{-3}$. We adopted this value to
 146 estimate the energy rate functions of the tremors.

147 We calculated the energy rate functions of the tremors by implementing the site
 148 amplification factors and Q^{-1} estimated by the above procedures. The energy rate function of a tremor
 149 ($E_j(t)$), estimated from the amplitudes of the j -th station, was calculated using the following equation:

$$150 \quad E_j(t) = 2\pi V_S r_j^2 \rho A''_j(t + t_j) \exp(2\pi f_c Q^{-1} t_j) \quad (2)$$

151 where, $A''_j(t)$ is the amplitude of envelopes after the site-correction at the j -th station, r_j is the
 152 hypocentral distance from the tremor source to the j -th station, t_j is the travel time from the tremor
 153 source to the j -th station, and ρ is the density (assuming 2,700 kg/m³ in this study). The epicentral
 154 locations of the tremors were set at those located by Yamashita et al. (2015, 2021). The depth of the
 155 tremors was set at the plate boundary of the JIVSM (Koketsu et al. 2012). To calculate the energy rate
 156 function, the time windows were set at 240 s, which started 60 s before the time window of the tremors
 157 set by Yamashita et al. (2015; 2021). We stacked the energy rate functions of a tremor for each station
 158 and estimated the average energy rate function $E_{ave}(t)$ divided by the number of stations used. We
 159 calculated the cross-correlation coefficients (CCs) of the energy rate functions of all station pairs in
 160 Fig. 4 and further utilized the stations whose CCs exceeded 0.6 with at least one other station when
 161 stacking the energy rate functions.

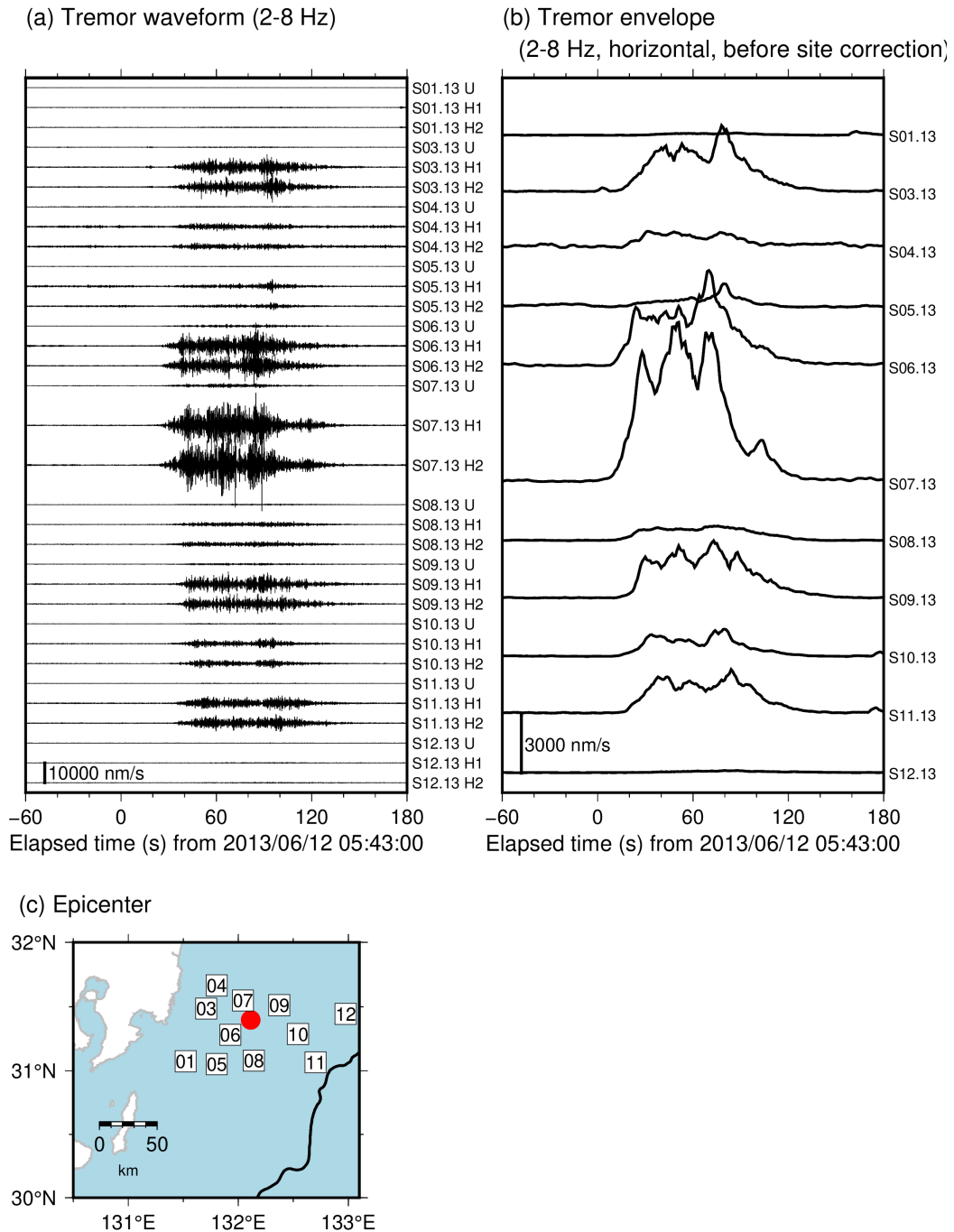
162 The seismic energy W of a tremor is calculated by integrating $E_{ave}(t)$ in the time range t_1 –
 163 t_2 :

$$164 \quad W = \int_{t_1}^{t_2} E_{ave}(t) dt. \quad (3)$$

165 The integration range is the period when the values of $E_{ave}(t)$ exceed 20% of the maximum value
 166 of $E_{ave}(t)$ (red line in the stacked energy rate function of Fig. 5). The duration of a tremor was
 167 defined as $t_2 - t_1$. The seismic energy rate of the tremor was estimated by dividing the seismic energy
 168 by the duration.

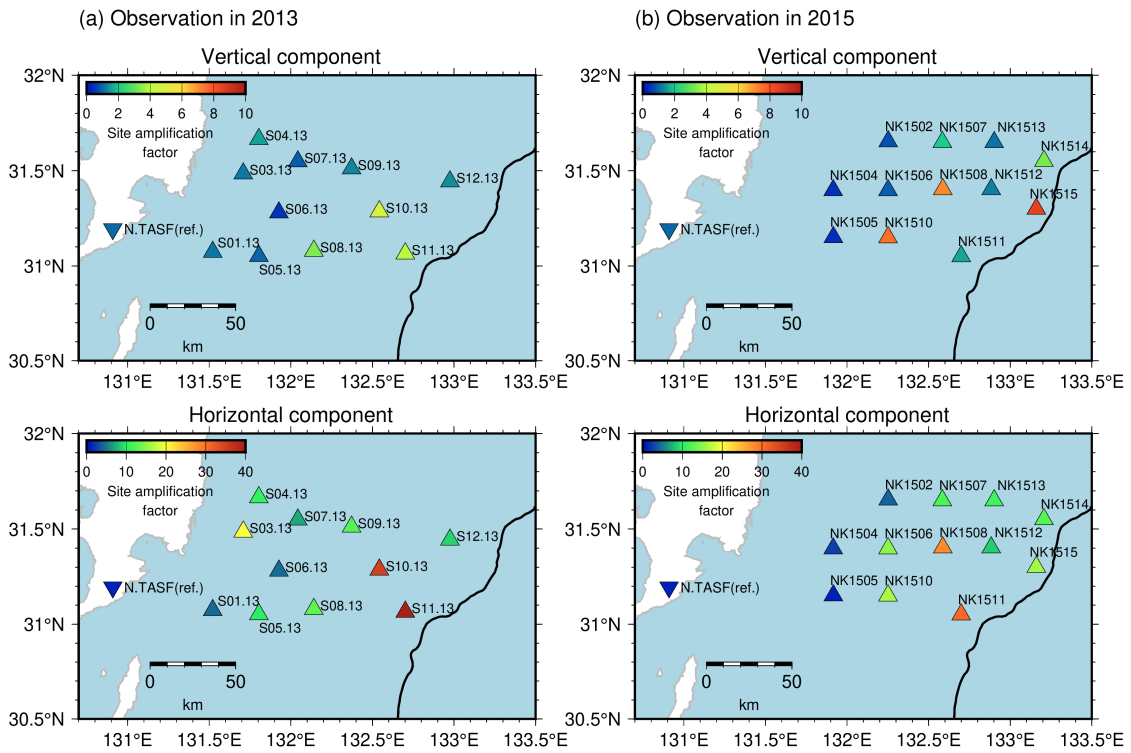
169

170



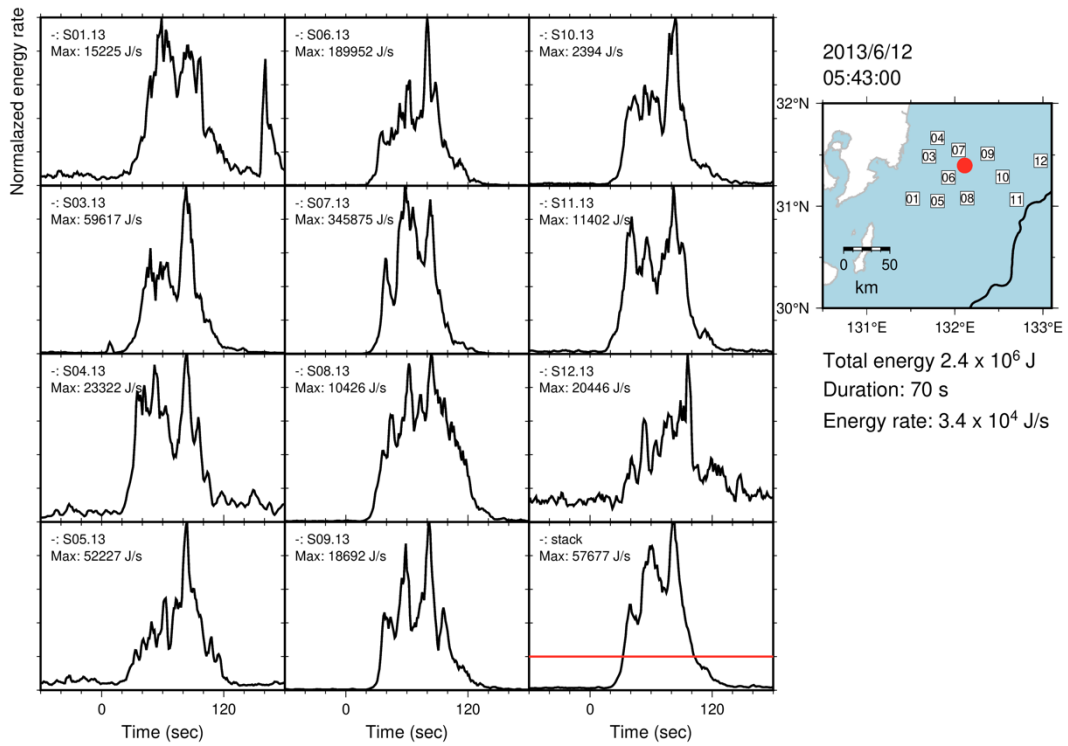
171
172
173
174
175
176
177
178

Figure 3. Example of (a) waveforms of a tremor in a frequency range of 2–8 Hz, and (b) envelopes obtained by the root-mean-square of sums squared seismograms of two horizontal components. Waveforms are displayed from 05:43:00 (JST, UTC+9), June 12, 2013. (c) Red circle depicts the epicentre of the tremor as displayed in in Fig. 3a and b. Black line represents the trench axis. Squares indicate the locations of OBSs.



179
 180
 181
 182
 183
 184

Figure 4. Site amplification factors relative to N.TASF. Triangles represent the locations of OBSs. Inverted triangle indicates the location of the F-net station, N.TASF. Black line is the same as displayed in Fig. 3. Estimation error of site amplification factors is shown in Fig. S2.



185

186

187 **Figure 5.** Temporal changes of energy rate functions of a tremor estimated at each OBS along with its

188 stacked energy rate function. Red line of the stacked energy rate function indicates the threshold,

189 which is set as 20% of the maximum value of the energy rate function. Red circle, squares and black

190 line are the same as displayed in Fig. 3.

191

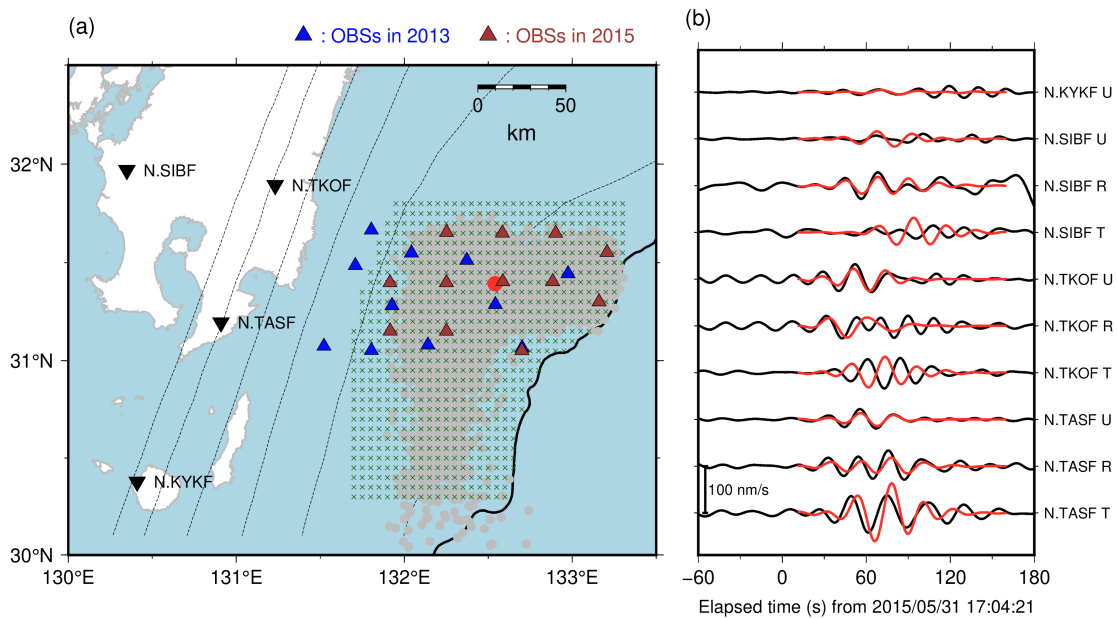
192 **2.2. Estimation of moments of VLFEs**

193 We estimated the source durations and seismic moments of VLFEs temporally
194 corresponding to the tremors in 2013 and 2015 detected by Yamashita et al. (2015; 2021) by comparing
195 observed and synthetic waveforms following the procedure of Yabe et al. (2021) and Baba et al. (2021).
196 We additionally estimated the source durations and seismic moments of VLFEs in 2010 detected by
197 Asano et al. (2015) using the same method. As long-period VLFE signals are difficult to recognize in
198 short-period OBS records, we utilized continuous seismograms at onshore broadband F-net stations
199 for estimation. Before the analysis, we removed the instrumental responses, resampled at one sample
200 per second, and applied a bandpass filter in a frequency range of 0.02–0.05 Hz to enhance the VLFE
201 signals.

202 To reduce the computational costs of calculating Green's functions, reciprocal calculations
203 were conducted using OpenSWPC (Maeda *et al.* 2017). We set source grids at an interval of 0.05° on
204 the plate boundary of the area where tremors were detected (Fig. 6a). The hypocentre of each VLFE
205 was assumed to be at the nearest grid from the hypocentre of the tremor located by Yamashita et al.
206 (2015; 2021) or at the hypocentre of VLFEs located by Asano et al. (2015). JIVSM was implemented
207 to calculate Green's functions. The minimum *S*-wave velocity in the elastic volume was set as 1.5
208 km/s. The model includes topography (ETOPO1; Amante & Eakins 2009), air, and seawater layers.
209 The default values of OpenSWPC were used for the density, seismic velocities, and quality factors in
210 seawater and air. The model volume was discretized using a uniform grid of 0.2 km. The focal
211 mechanisms were assumed to be consistent with the geometry of the plate boundary model of JIVSM
212 and the plate convergence direction of the plate motion model NUVEL-1A (DeMets *et al.* 1994). By
213 combining the assumed focal mechanisms and Green's functions, we prepared a series of synthetic
214 velocity seismograms with triangular functions and source durations of 10–50 s (e.g., Takemura et al.,
215 2019).

216 We calculated the station- and component-averaged CCs between the synthetic and observed
217 waveforms in a time window of 150 s from the assumed origin time of a VLFE. The origin time was
218 searched for in the range from 30 s before to 30 s after the start time of the duration range of the
219 temporally corresponding tremor or the origin time of VLFEs located by Asano et al. (2015). The fit
220 between the observed and simulated Love waves was not sufficient compared with the Rayleigh wave
221 (Fig. 6b). It may be inferred that the sedimentary structure of JIVSM at very shallow depths (< 5 km)
222 in Hyuga-nada is insufficient to simulate Love waves, which are sensitive to shallow structures. We
223 verified that the CCs between the simulated and observed waveforms of a regular earthquake located
224 by Takemura et al. (2020) in the transverse components were also low, whereas those in the vertical
225 and radial components were high (Fig. S3). Therefore, we used only the vertical and radial components
226 (Rayleigh waves) when calculating the CCs. For the N.KYKF station, only the vertical component
227 was utilized because the horizontal components were noisy. The combination of source duration and

228 origin time, with the highest average CC in the grid search, was adopted. We calculated the relative
 229 amplitudes by minimizing the variance reduction between simulated and observed waveforms (Baba
 230 et al. 2021; Yabe et al. 2021), and further estimated the seismic moments of VLFs using the estimated
 231 relative amplitudes. The moment, duration, and average CC of the example in Fig. 6 were 2.0×10^{15}
 232 Nm, 24 s, and 0.65, respectively. Events with average CCs smaller than 0.3 were discarded. The
 233 seismic moment rate of the VLF was obtained by dividing the seismic moment by the source duration.
 234



235

236

237 **Figure 6.** (a) VLFE source grids for the VLFE analysis. Green crosses indicate the locations of the
 238 VLFE source grids. Gray dots indicate the epicentres of tremors detected by Yamashita et al. (2015;
 239 2021). Red circle indicates the epicentre of the event displayed in Fig. 6b. Blue and brown triangles
 240 depict the locations of OBSs in 2013 and 2015, respectively. Dashed contours indicate the isodepth of
 241 the top of the Philippine Sea plate at 10-km intervals (JIVSM; Koketsu et al. 2012). Black line
 242 represents the trench axis. Inverted triangles display the locations of the F-net stations. (b) An example
 243 of a VLFE in a frequency range of 0.02–0.05 Hz. Waveforms are depicted from 17:04:21 (JST,
 244 UTC+9), May 31, 2015. Black and red lines are the observed and the simulated waveforms,
 245 respectively. R, T, and U components represent the radial, transverse, and vertical components,
 246 respectively.

247

248 **3. Results**

249 We estimated the energies of 1,672 and 6,126 shallow tremors in 2013 and 2015,
250 respectively. We classified the analysis region into three areas based on spatial variation in slow
251 earthquake activity: Area A, south of 31.0° N; Area B, west of 132.4°E, north of 31.0° N; and Area C,
252 east of 132.4°E, north of 31.0° N (see rectangles of Figs 7 and 8). Area A is south of the subducted
253 Kyushu-Palau Ridge, Area B is near the top of the subducted ridge, and Area C is east of the subducted
254 ridge. Most of Areas A and C are outside the subducted ridge. In 2013, tremors and VLFES occurred
255 mainly in Areas A and B, whereas in 2015, they occurred mainly in Areas B and C. The dominant
256 range of tremor energies was 10^4 – 10^8 J with spatial variation (Fig. 7). In 2013 (Fig. 7a), tremors with
257 large energies ($> 10^{6.5}$ J) were concentrated in Area A. This characteristic is confirmed in the maximum
258 and medium values of tremor energies (Fig. S4a). In 2015 (Fig. 7b), tremors with larger energies ($>$
259 10^7 J) occurred near the north-eastern edge of the subducted Kyushu-Palau Ridge in Area C. The
260 tremor energies near the trench axis in Area C were smaller. These characteristics are also shown in
261 the maximum tremor energies (Fig. S4b). Although median tremor energies are small in the longitude
262 of 132.5°–132.7° due to the detection of many small events, the north-eastern edge of the subducted
263 Kyushu-Palau Ridge in Area C is considered as large tremor energy area.

264 The moments were also estimated for 1,297, 904, and 1,785 shallow VLFES in 2010, 2013,
265 and 2015, respectively. The dominant range of the VLFE moments was $10^{13.5}$ – $10^{16.5}$ Nm (Fig. 8).
266 South of 31.0° N (Area A), VLFES with large moments ($> 10^{15.5}$ Nm) occurred in 2010 and 2013 (Fig.
267 8ab). North of 31.0° N, VLFES extended near the trench axis in 2010 and 2015. In particular, VLFES
268 with large moments ($> 10^{15.5}$ Nm) in 2010 and 2015 (Figs 8a and c) are concentrated east of 132.4° E
269 (Area C). In the west of 132.4° E and north of 31.0° N (Area B), the VLFE moments are relatively
270 small. These observations are stably confirmed in the maximum and medium values of VLFE
271 moments (Fig. S4c-f). The spatial variations in the VLFE moments and tremor energies for each
272 observation period were similar (Figs 7 and 8). The spatial variations in the energy rates of tremors
273 and moment rates of VLFES were also similar to those of tremor energies and VLFE moments (Figs
274 S6 and S7). We summarized our observations: the energies of the tremors and moments of VLFES are
275 generally larger outside the subducted ridge (Areas A and C) than near the top of the subducted ridge
276 (Area B).

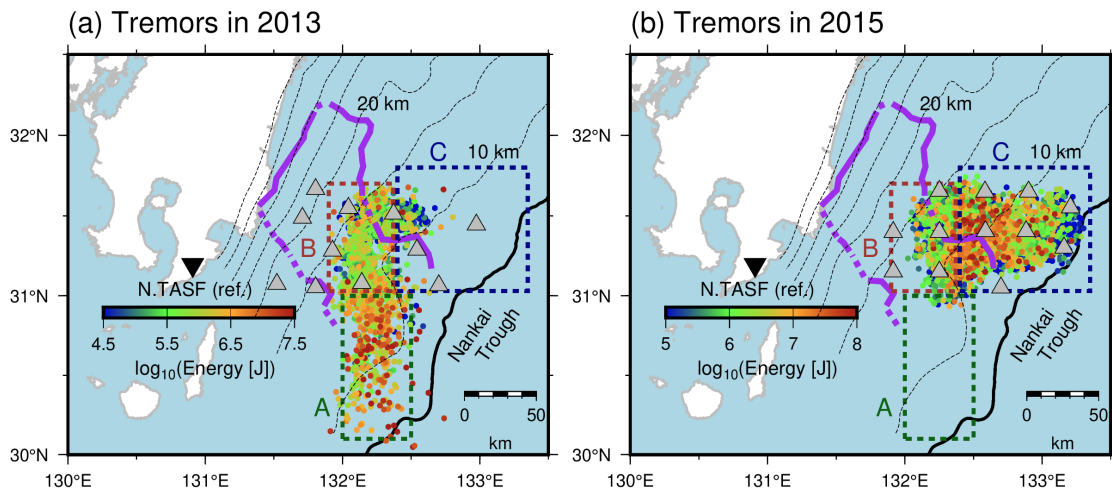
277 The spatiotemporal variation in moments and energies of slow earthquakes and the change
278 in the migration speed are associated (Fig. 9a and b). Hereafter, we mainly discuss the spatiotemporal
279 variation in slow earthquakes based on VLFE activity because the spatiotemporal variations in VLFE
280 moments and tremor energies were similar, and the VLFE analysis covered all episodes in 2010, 2013,
281 and 2015. Here, we summarized migration patterns in each episode. Their detailed features were
282 described in the previous studies (Asano et al. 2015; Yamashita et al. 2015; Yamashita et al. 2021).
283 The episodes in 2010 and 2015 are divided into three migrations and the 2013 episode is divided into

284 two migrations (Fig. S8 and Table S1). The 2010a, 2013a, and 2013b migrations were northward along
285 the strike, whereas the 2010b, 2010c, 2015a, 2015b, and 2015c migrations were along the dip with
286 variable directions (Figs 9 and S8; Table S1). All migrations along the strike direction consistently
287 started in Area A (Figs 9b, S8a, S8d, and S8e). Subsequently, the VLFs migrated northward and
288 entered the subducted ridge. After VLFs entered Area B, their migration speed became slow (Fig. 9a
289 and b). The spatiotemporal variation in the migration front seems to be parabolic (discussed in detail
290 in Section 4.1). Rapid tremor reversals (RTRs; black dotted arrows in Figs 9b and S8d), which is a
291 fast backward migration (e.g., Houston et al. 2011), occurred during the migration in 2013.

292 In the main front of along-strike migrations, the moments of VLFs become smaller after
293 the front entered the Area B and the migration speed slowed (Figs 9b, S8a, S8d, and S8e). Therefore,
294 the migration speed and the moments of VLFs are positively correlated. On the other hand, the
295 moments of the VLFs in RTRs become larger when RTRs entered Area A (Figs 9b and S8d). This
296 suggests that the moments of VLFs depend on the location.

297 In the downdip of shallow tremors and VLFs, repeating earthquakes occurred at depths of
298 15–30 km. The repeating earthquake activity manifests that the plate boundary around the patch is
299 creeping; therefore, the large slip rate by repeating earthquakes suggests that the interplate coupling is
300 weak (e.g., Uchida & Matsuzawa 2011). Fig. 10 compares the spatial distributions of slip rates from
301 repeating earthquakes and cumulative moments of VLFs. Cumulative moments of VLFs may be
302 also linked with the strength of interplate coupling (Baba *et al.* 2020). The interplate slip rate estimated
303 from repeating earthquakes was higher in the south along the strike direction (Yamashita et al. 2012);
304 therefore, the interplate coupling may be weaker at depths of 15–30 km in the south (downdip part of
305 Area A) than in the north (downdip of Area B). The cumulative moment of shallow VLFs in 2010
306 and 2013, episodes with along-strike migrations, was also smaller in Area B than in Area A during the
307 episodes (Fig. 10). Baba et al. (2020) found the tendency that cumulative moment of shallow VLFs
308 was larger in areas with weak interplate coupling along the Nankai Trough. In Hyuga-nada, the slip
309 rate of repeating earthquakes and the cumulative moment of VLFs are larger in the south (in and
310 downdip of Area A) than in the north (in and downdip of Area B). These observations suggest that
311 although there is a difference in the slip behaviour along the dip direction, such as repeating
312 earthquakes and VLFs, the interplate coupling may be consistently weak in the south along the strike
313 direction.

314



315

316

317

318

319

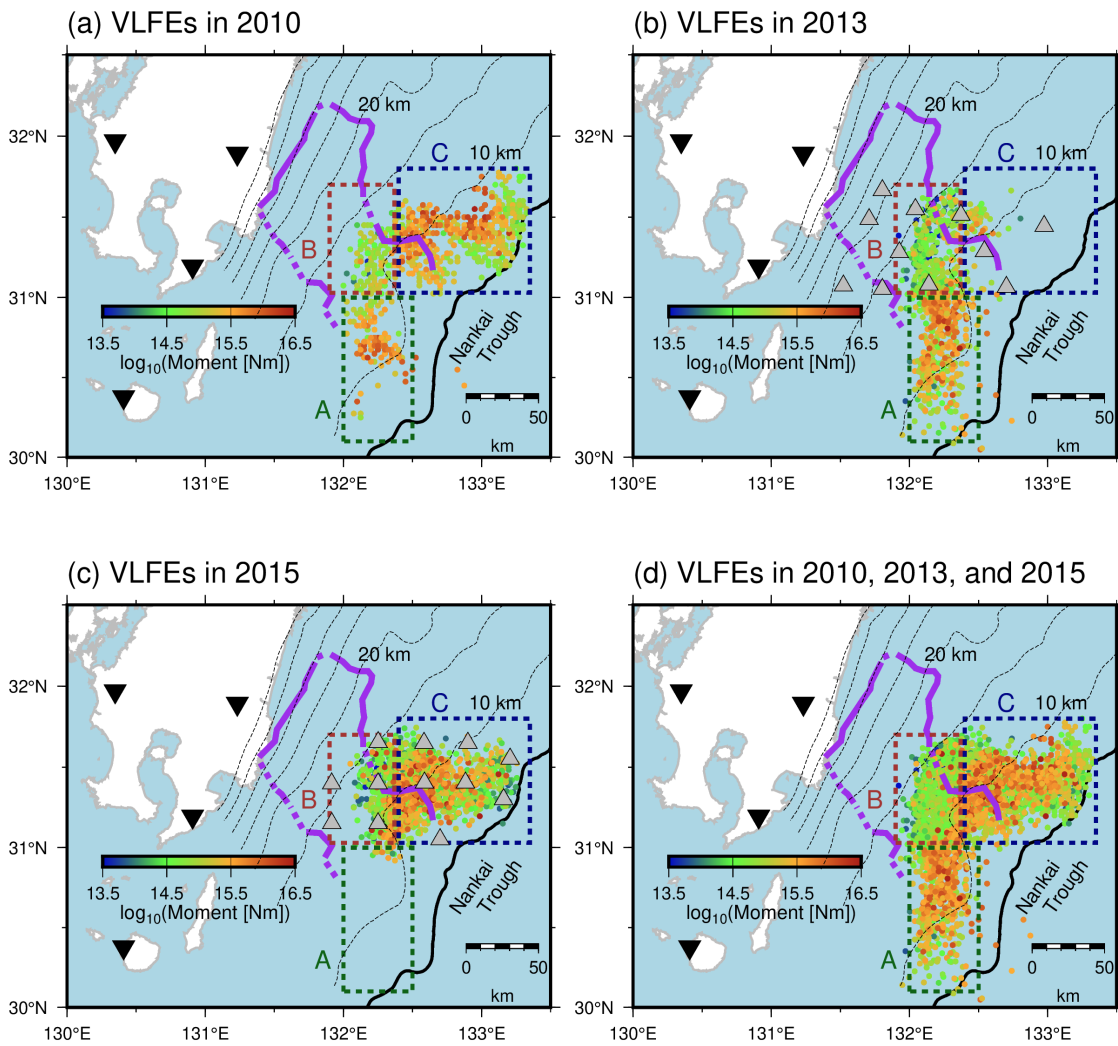
320

321

322

323

Figure 7. Spatial distribution of energies of shallow tremors (a) in 2013 and (b) in 2015. Green, brown, and dark blue dotted rectangles indicate the ranges of Area A, B, and C, respectively. Purple lines represent the inferred subducted Kyushu-Palau Ridge (Yamamoto *et al.* 2013). Gray triangles depict the locations of OBSs. Inverted triangles and black line are the same as displayed in Fig. 3. Dashed contours indicate the isodepth at the top of the Philippine Sea plate in intervals of 5 km (Nakanishi *et al.* 2018).



324

325

326 **Figure 8.** Spatial distribution of moments of shallow VLFs in (a) 2010, (b) 2013, (c) 2015, and (d)

327 all analysis periods. Coloured dotted rectangles, dashed contours, purple lines, black line and grey

328 triangles are the same as displayed in Fig. 7.

329

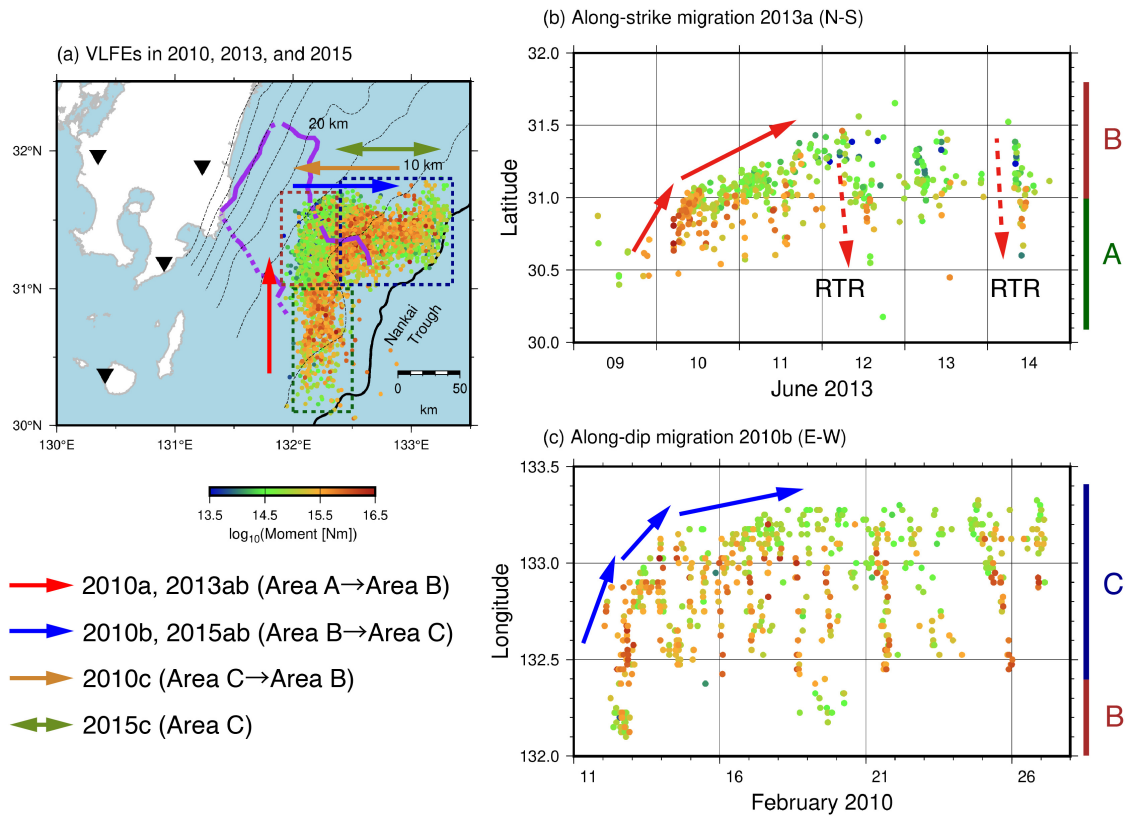
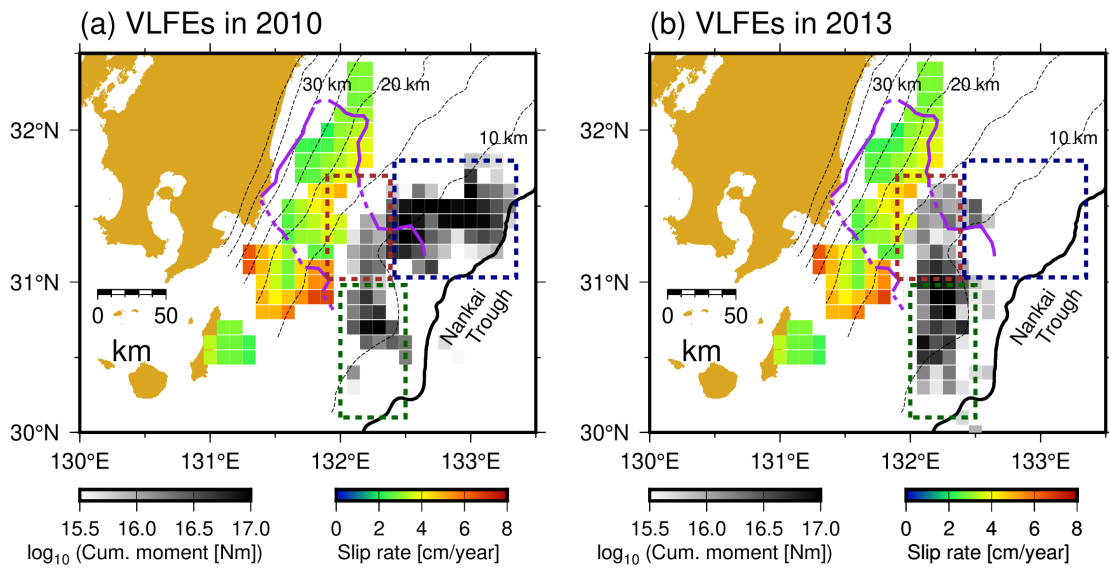


Figure 9. (a) Summary of slow earthquake migration patterns. Coloured arrows represent the direction of migration patterns. Coloured dotted rectangles, dashed contours, purple lines and black inverted triangles are the same as displayed in Fig. 8. (b) Spatiotemporal distributions of (b) an along-strike migration 2013a and (c) along-dip migration 2010b with moments of VLFEs. Black arrows indicate the direction of migrations. Black dotted arrows in Fig. 9b represents the RTR.



338

339 **Figure 10.** Relationship between slip rates estimated from repeating earthquakes (Yamashita et al.
340 2012) and shallow slow earthquakes. Gray scales exhibit the cumulative moments of VLFs. Colour
341 scale indicates the slip rate estimated from repeating earthquakes. Coloured dotted rectangles, purple
342 lines, black lines, and dashed contours are the same as in Fig. 8.

343

344

345 **4. Discussion**

346 **4.1. Along-strike spatial variation in slow earthquake activity**

347 To investigate the controlling factor of the along-strike variation in slow earthquake activity
348 in Hyuga-nada, we compared the activity with a physical model of along-strike slow earthquake
349 migration by Ando et al. (2012). In their model, high- and low-strength brittle tremor patches exist on
350 the ductile background based on Newtonian rheology. These brittle patches are triggered by the stress
351 increase at the migration front of an SSE. They predicted that ETS starts migrating energetically in
352 areas with high tremor-patch strength (strong patch areas) and decelerates with a parabolic
353 spatiotemporal pattern in areas with low-tremor patch strength (weak patch areas). In Hyuga-nada, the
354 migration speed was faster, and the VLFE moment was larger in Area A than in Area B (Fig. 9). These
355 observations are consistent with the modelling results by Ando et al. (2012). The along-strike variation
356 in slow earthquake activity in Hyuga-nada can be explained by the difference in the patch strength of
357 slow earthquakes, where Areas A and B are considered strong and weak patch areas, respectively.

358 The spatial variations in tremor activity in Shikoku and VLFE activity off the south-eastern
359 Kii Peninsula were also discussed based on Ando et al. (2012) (Shikoku: Kano et al. 2018b; off the
360 southeast Kii Peninsula: Yamamoto et al. 2022). In Shikoku, western and central Shikoku were
361 interpreted as strong and weak patch areas, respectively, whereas the areas west of and inside the
362 subducted Paleo-Zenisu ridge off the Kii Peninsula were regarded as strong and weak patch areas,
363 respectively.

364 A possible factor for the along-strike spatial variation in slow earthquake activity in Hyuga-
365 nada is the heterogeneity of pore fluid pressure. Kano et al. (2018b) suggested that the heterogeneity
366 of strong and weak patch areas is caused by the variation in effective normal stress, which is associated
367 with that in the fluid pressure on the plate boundary. Takemura et al. (2022a) discussed that the
368 variation in the pore fluid pressure can induce the change of the migration speed, which can be
369 considered as a proxy for rupture propagation of an SSE (e.g., Bartlow et al. 2011; Ito et al. 2007), off
370 the Cape Muroto and Kii Peninsula. In Hyuga-nada, the change in migration speed between Area A
371 and B may be caused by the pore fluid pressure heterogeneity. To discuss the variation in the pore fluid
372 pressure in Hyuga-nada in more detail, investigations of seismic velocity structures (especially V_p and
373 V_p/V_s ratio) are required in future work.

374 Another possible factor is the geometrical effects of the subduction of a ridge. Wang and
375 Bilek (2011) suggested that a fracture network caused by a subducted seamount generates structural
376 and stress heterogeneities. According to Chesley et al. (2021), the subduction of a seamount can
377 transport considerable volume of fluid to forearc and complex fracture network, which can generate
378 the effective normal stress variation. Takemura et al. (2022b) and Yamamoto et al. (2022) suggested
379 the variation in cumulative moments of VLFEs which is associated with subducted Paleo-Zenisu ridge
380 off the Kii Peninsula. In Hyuga-nada, the subduction of the Kyushu-Palau ridge may also generate the

381 stress heterogeneity on the plate boundary.

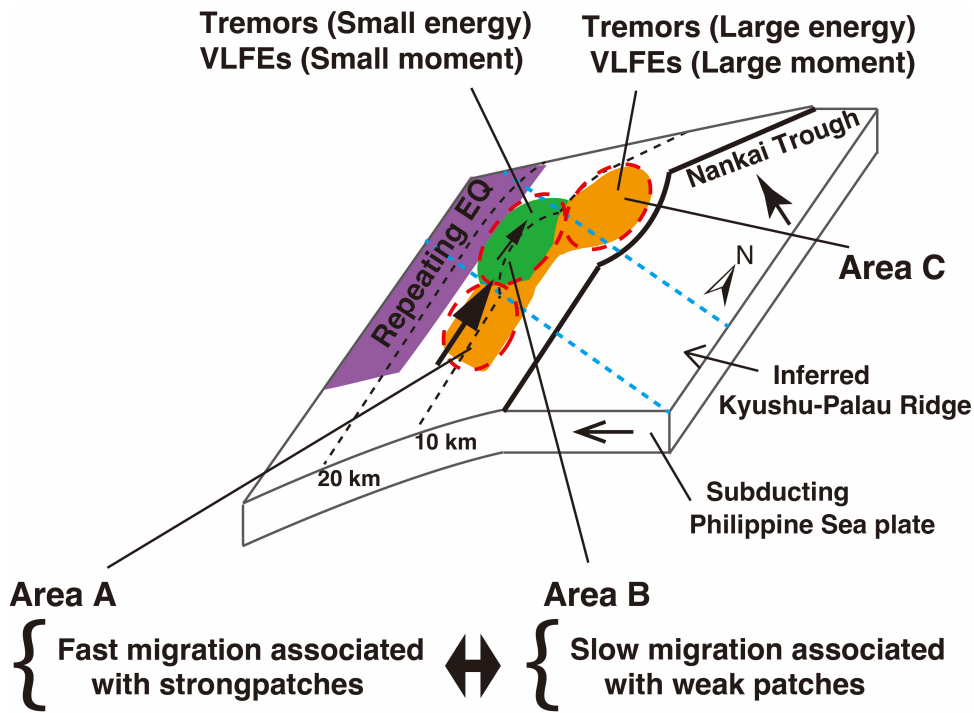
382 As mentioned in Section 3, the spatiotemporal variation in the migration front appears to be
 383 parabolic. Following Ando et al. (2012), we investigated which function is better for fitting the
 384 migration front in 2013a, exponential ($t=C \exp(x)$; t is the elapsed time, x is the migration distance,
 385 and C is constant) or parabolic ($t=D^{-1}x^2$; D is the diffusion coefficient). Although tremor epicentres
 386 were scattered around the start of migration, the migration pattern seems to be better fitted by a
 387 parabola (Fig. 12) rather than exponential, and the diffusion coefficient D is evaluated as $\sim 6 \times 10^4 \text{ m}^2/\text{s}$.

388 Ando et al. (2012) assumed that fault strength is equals to τ_p when slip velocity $v=0$ and
 389 equals to $\tau_r + \eta v$ when $v > 0$ following Ando et al. (2010) and Nakata et al. (2011). τ_p , τ_r , η are peak
 390 strength, residual strength, and viscosity factor, respectively. In Ando et al. (2012), τ_r is set as zero and
 391 the patch strength is represented by τ_p . The difference in τ_p between strong and weak patches is
 392 supposed to be represented by that in stress drop. Therefore, we evaluated the variation in the stress
 393 drop of the VLFES in Hyuga-nada. Assuming a circular crack model, the seismic moment M_0 of an
 394 earthquake is given by (e.g., Kanamori & Anderson 1975):

$$395 \quad M_0 = \frac{16}{7} \Delta\tau r^3 \quad (4)$$

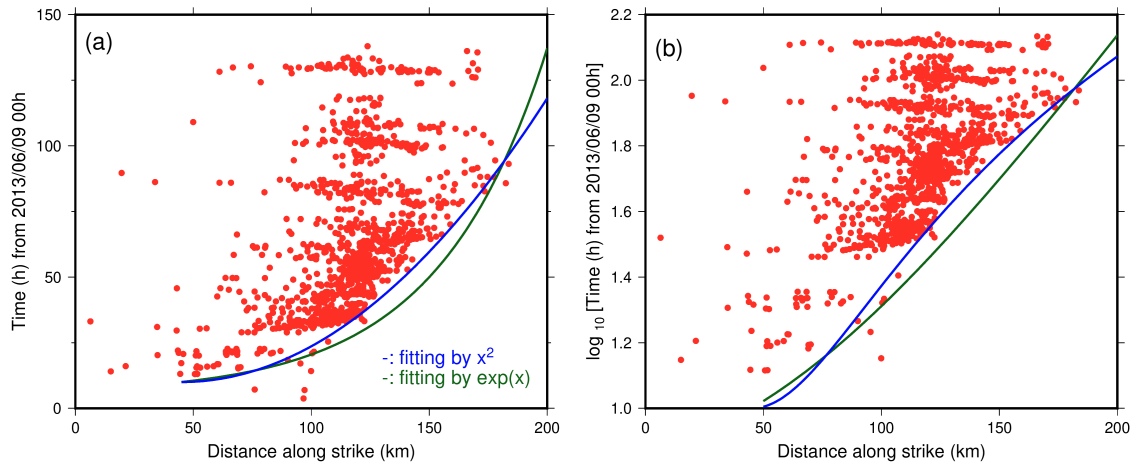
396 where $\Delta\tau$ is the stress drop and r is the radius of the patch. In this section, this relationship is further
 397 assumed in VLFES. The average moment of a VLFE in Area A (strong patch area) and in Area B (weak
 398 patch area) is $3.3 \times 10^{15} \text{ Nm}$ and $1.1 \times 10^{15} \text{ Nm}$, respectively (Fig. 8). Considering Ohta & Ide (2017)
 399 estimated the source radius of a deep VLFE with $M_0 = 1.2 \times 10^{14} \text{ Nm}$ as $\sim 5 \text{ km}$, we assume the radius of
 400 a shallow VLFE patch in Hyuga-nada with $M_0 = 10^{13.5} - 10^{16.5}$ as 3–30 km. If patches with a radius r of
 401 3–30 km are assumed, the average stress drop of a VLFE in Areas A and B is evaluated as $5.3 \times 10^1 -$
 402 $5.3 \times 10^4 \text{ Pa}$ and $1.8 \times 10^1 - 1.8 \times 10^4 \text{ kPa}$, respectively. The spatiotemporal distribution of migration is
 403 parabolic if the difference in stress drop between strong and weak patches is sufficient (Ando et al.
 404 2012). As indicated by the fitting of the migration front, the spatiotemporal variation in the slow
 405 earthquake migration front was parabolic (Fig. 9b). Although the model of Ando et al. (2012) assumed
 406 an 11-times differences between strong and weak patches, if the patch size in Areas A and B is similar,
 407 parabolic migration pattern was observed by an approximately three-time difference in the stress drops
 408 of these patches in Hyuga-nada. On the other hand, since the difference in the moment of VLFES
 409 between Areas A and B may be due to the patch size, slip distribution of VLFES should be investigated
 410 in future studies. However, the estimation of slip areas of shallow VLFES is a challenging issue due
 411 to offshore heterogeneities along the propagation path. The patch heterogeneity may be a key factor
 412 of variations in tremor energy, VLFE moment, and migration speed in Hyuga-nada.

413



414
415
416
417
418
419

Figure 11. Schematic illustration of the interpretation of distributions of slow earthquakes and Kyushu-Palau Ridge.



420
421
422
423
424
425
426

Figure 12. (a) Spatiotemporal distribution of tremor migration in the episode of 2013a. Vertical and horizontal axis shows the elapsed time from 2013/06/09 00:00:00 JST, and Distance along the strike (N-S) from 30.0°N, respectively. Blue and green lines indicate the parabolic and exponential curves, respectively. (b) Same as (a) but the vertical axis is log-scale.

427 **4.2. Scaled energy of shallow slow earthquakes in Hyuga-nada**

428 Recently, slow earthquake signals have been also detected in the microseism frequency band
 429 between tremors and VLFEs (Kaneko et al. 2018; Masuda et al. 2020; Yamashita et al. 2021); therefore,
 430 slow earthquakes are assumed to be broadband phenomena. To investigate the characteristics of
 431 broadband slow earthquakes, we evaluated the scaled energy of the slow earthquakes in Hyuga-nada.
 432 Ide et al. (2008) demonstrated the seismic energy rates of slow earthquakes in 2–8 Hz are proportional
 433 to the seismic moment rates and evaluated the scaled energy of slow earthquakes by the ratio between
 434 tremor energy rate and the accompanying VLFE moment rate. Scaled energy has been used for the
 435 purpose of comparing dynamic characteristics of earthquakes in different tectonic setting (Kanamori
 436 & Rivera 2006). If the rupture process of seismic events is self-similar, the scaled energy is constant.
 437 Previous studies demonstrated that scaled energy of slow earthquakes is 10^{-10} – 10^{-8} and 4–5 orders
 438 smaller than that of regular earthquakes (e.g., Ide et al. 2008). Following previous studies, we
 439 estimated the scaled energy using the ratio between the tremor energy rate and VLFE moment rate for
 440 activities in 2013 and 2015, when the energy rate could be estimated from the OBS records.

441 The dominant range of the scaled energy was 10^{-11} – 10^{-8} both in 2013 and 2015 (Fig. 13ab).
 442 Although the distribution of the median scaled energy is smaller around the eastern edge of the
 443 Kyushu-Palau Ridge in Area C, the range of the median scaled energy is in the range of 10^{-10} – 10^{-9} in
 444 all areas (Fig. 13cd); therefore, the spatial variation in the median scaled energy is similar in the order
 445 scale. Dominant ranges of scaled energies did not change significantly between episodes in 2013 and
 446 2015 (Fig. S9). The range of scaled energies in Hyuga-nada is similar to or one order smaller compared
 447 to the off the Cape Muroto and Kii Peninsula (10^{-10} – 10^{-8} ; Yabe et al. 2021, 2019), along the Japan
 448 Trench (10^{-10} – 10^{-9} ; Yabe et al. 2021), and in Costa Rica (10^{-9} – 10^{-8} ; Baba et al. 2021). The range of
 449 scaled energies of shallow slow earthquakes in Hyuga-nada is also similar to those of deep slow
 450 earthquakes in southwest Japan, Cascadia, and Mexico ($10^{-9.5}$ – 10^{-9} ; Ide, 2016; Ide and Maury, 2018;
 451 Ide and Yabe, 2014; Fig. 14). However, the range of scaled energy in Hyuga-nada is broader than other
 452 slow earthquake regions.

453 Ide (2008) and Ide & Maury (2018) discussed the theoretical relationship between seismic
 454 energy and seismic moment of slow earthquakes by the Brownian slow earthquake model. In their
 455 model, the characteristic size of the slip area S is described by:

456
$$S = Cr^2 \quad (5)$$

457 where r is a random variable and C is a constant. The temporal change of r is described by:

458
$$dr = -\alpha r dt + \sigma dB \quad (6)$$

459 where α is the characteristic frequency of slow earthquakes (α^{-1} is a characteristic time), dB is the
 460 random variable of Gaussian distribution with the mean 0 and the variance 1, σ is the fluctuation
 461 magnitude. They discussed that the energy rate divided by the square of the moment rate depends on
 462 a characteristic frequency of a slow earthquake event, α :

463

$$\frac{E[E_{rate}]}{E[M_{rate}]^2} = \frac{4\alpha}{5\pi\rho V_s^5 \Delta t} \quad (7)$$

464

where ρ is the density, V_s is the S -wave velocity, and Δt is the time steps of the stochastic process.

465

$E[E_{rate}]$ and $E[M_{rate}]$ indicates the long-term averages of energy rates and moment rates, respectively.

466

Ide & Maury (2018) evaluated $E[E_{rate}]/E[M_{rate}]^2$ and α^{-1} of seismic slow earthquakes in deep southwest

467

Japan, Cascadia, and Mexico as 10^{-22} – 10^{-20} and 0.3–30 s, respectively. The range of α^{-1} of the SSE

468

scale in deep southwest Japan, Cascadia, and Mexico evaluated by Ide & Maury (2018) is 75–300 s.

469

$E[E_{rate}]/E[M_{rate}]^2$ in Hyuga-nada is estimated to be $10^{-24.5}$ – 10^{-21} (Figure S10). Although the small value

470

of $E[E_{rate}]/E[M_{rate}]^2$ is possibly caused by because the ρ and/or V_s may be smaller in Hyuga-nada, if ρ ,

471

V_s , and Δt is the same order as in the values of Ide & Maury (2018), α^{-1} in Hyuga-nada is estimated to

472

be 3–10000 s. In Hyuga-nada, there may be slow earthquake events that have similar or longer

473

characteristic times than those of other slow earthquake regions. In addition, the range of the

474

characteristic time is broader in Hyuga-nada than in other slow earthquake regions; therefore, slow

475

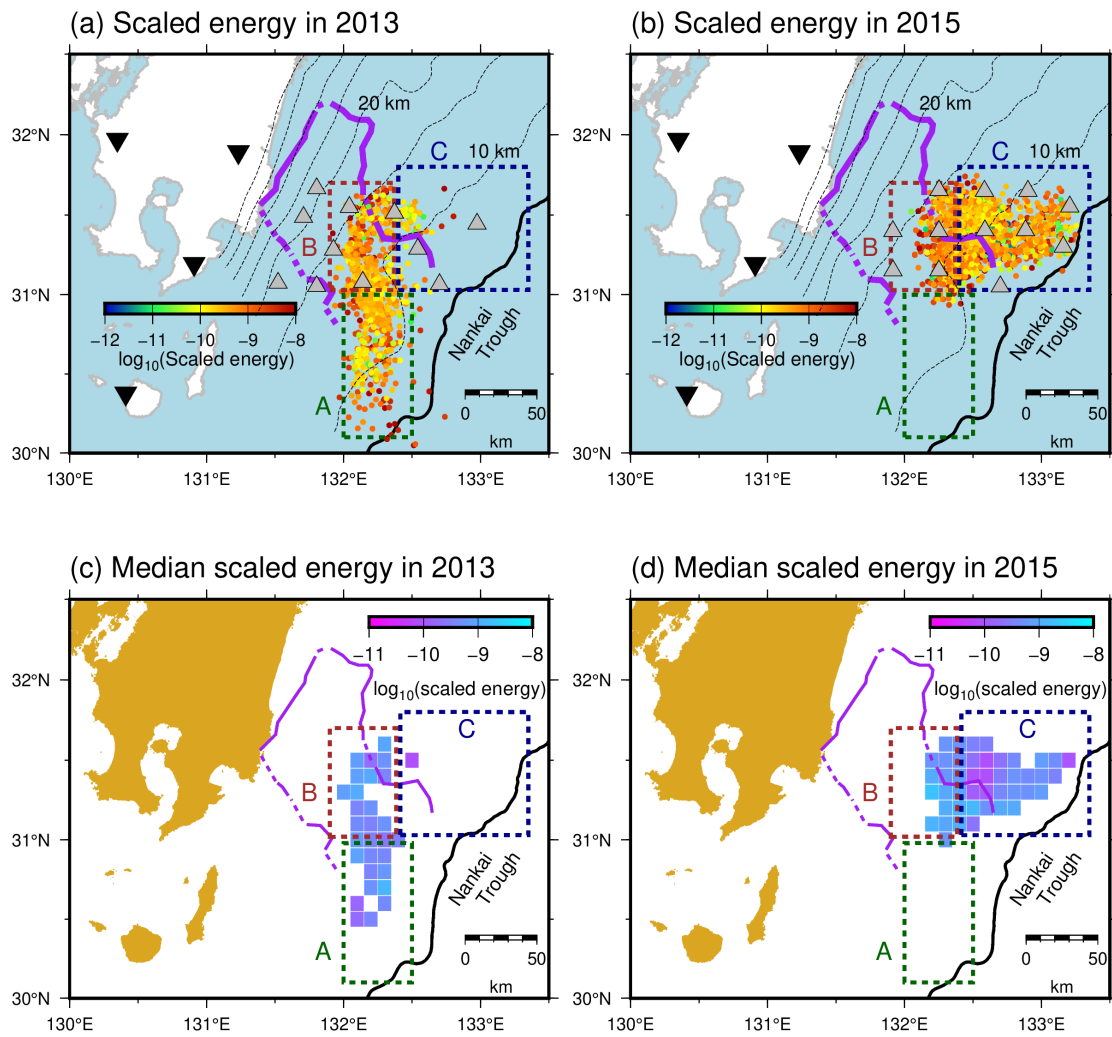
earthquakes in Hyuga-nada may have various spectral features. Based on Ide & Maury (2018), the

476

wide range of characteristic time in this area suggests width variations of tremor source area.

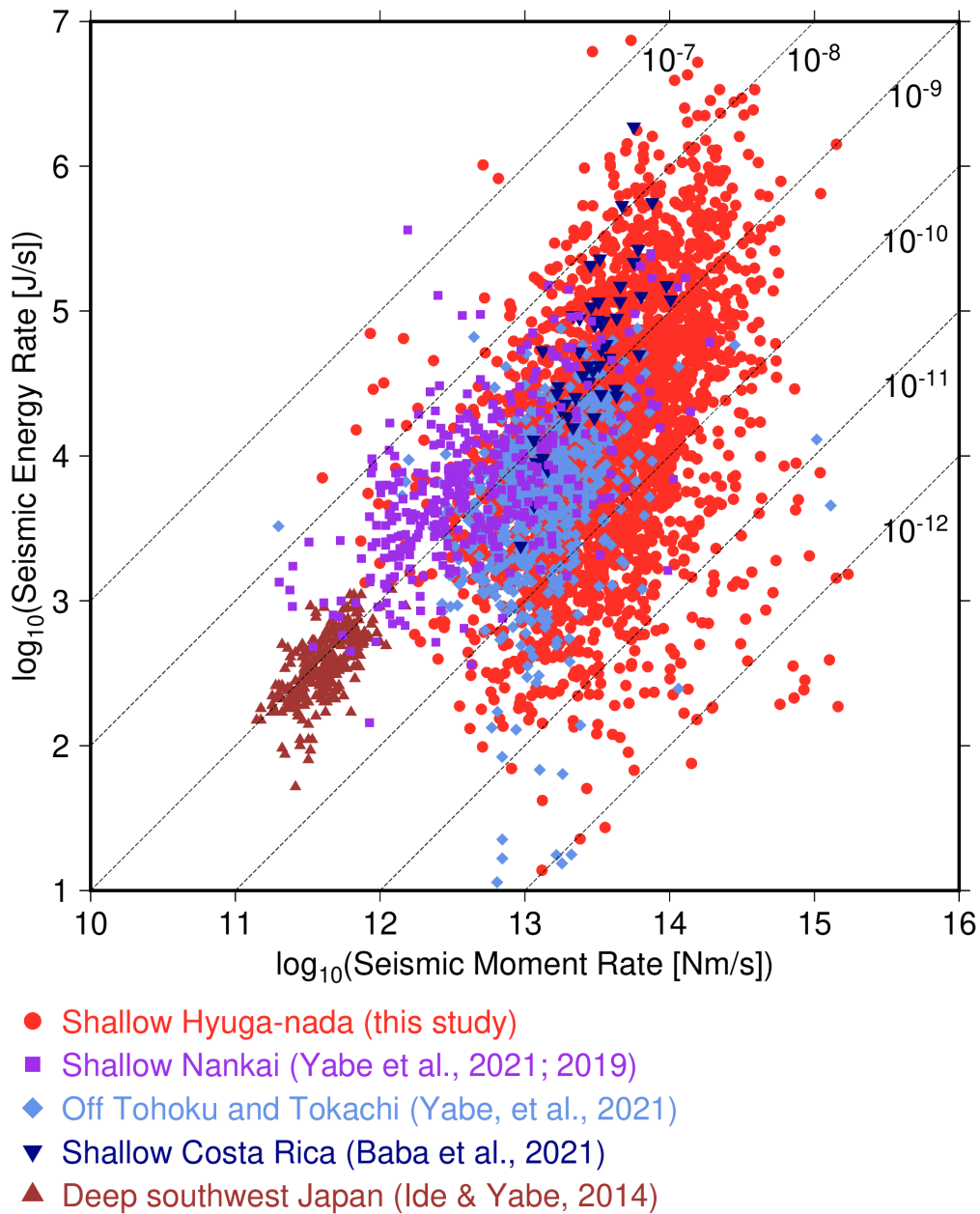
477

478



479
 480
 481
 482
 483
 484
 485

Figure 13. Spatial distribution of scaled energy of shallow slow earthquakes (a) in 2013 and (b) in 2015. Spatial distribution of the median scaled energy in the grid of $1^\circ \times 1^\circ$ where the number of event is larger than 10 (a) in 2013 and (b) in 2015. Coloured dotted rectangles, purple lines, black lines, grey triangles, inverted triangles, and dashed contours are the same as in Fig. 8.



486

487

488 **Figure 14.** Relationship between seismic moment rates of VLFs and seismic moment rates of tremors.

489 Red circles, purple squares, green diamonds, dark blue inverted triangles, and dark blue triangles

490 indicate the relationships between seismic moment rates of VLFs and seismic moment rates of

491 tremors in shallow Hyuga-nada (this study), shallow Nankai except Hyuga-nada (Yabe *et al.* 2019,

492 2021), off Tohoku and Tokachi (Yabe *et al.* 2021), shallow Costa Rica (Baba *et al.* 2021), and deep

493 slow earthquakes (Ide & Yabe 2014; Ide 2016; Ide & Maury 2018). Dashed lines represent scaled

494 energies of 10^{-7} , 10^{-8} , 10^{-9} , 10^{-10} , 10^{-11} , and 10^{-12} .

495

496 **5. Conclusion**

497 To investigate the spatial variation in the source characteristics of shallow slow
498 earthquakes in Hyuga-nada at a higher resolution, we estimated the energies of shallow tremors,
499 moments of shallow VLFs, and the scaled energy of shallow slow earthquakes in Hyuga-nada using
500 the data from permanent onshore broadband and temporary offshore seismometers. The dominant
501 ranges of energies of tremors and moments of VLFs are 10^4 – 10^8 J and $10^{13.5}$ – $10^{16.5}$ Nm/s,
502 respectively. The energies of tremors and moments of VLFs are larger in Areas A and C (most of
503 which are outside the subducted Kyushu-Palau Ridge) than in Area B (near the top of the subducted
504 ridge). The migration of tremors and VLFs along the strike direction started in Area A (south of the
505 subducted ridge) with events of larger tremor energies and VLF moments. After going north and
506 entering Area B (near the top of the subducted ridge), the migration speed slowed, and the tremor
507 energies and VLF moments were observed to be small (Fig. 9b).

508 Based on the physical model of Ando et al. (2012), strengths of slow earthquake patches
509 in Areas A and B are expected to be strong and weak, respectively. The spatiotemporal distribution of
510 the tremor migration in 2013 is fitted by a parabolic function with the large energy and moment events
511 at the initiation of the migration in Area A. If a circular crack model and same patch sizes are assumed,
512 the difference in average stress drop of the VLFs in Area A (strong patch) and Area B (weak patch)
513 is evaluated as three times. This difference in the stress drop of strong and weak patches may generate
514 a parabolic migration pattern. The along-strike variation in the rupture process on the plate boundary,
515 such as the stress drop, in slow earthquake regions can cause variations in the moment of slow
516 earthquakes and migration pattern near the southern edge of the subducted ridge.

517 The dominant range of scaled energy of slow earthquakes in Hyuga-nada is estimated as
518 10^{-11} – 10^{-8} . The range of scaled energies in Hyuga-nada is similar to or one order smaller than other
519 slow earthquake regions. Furthermore, this range is broader than other regions. Based on the Brownian
520 slow earthquake model by Ide & Maury (2018), the characteristic times of slow earthquakes in Hyuga-
521 nada (3–10000 s) is similar to or longer than those of other slow earthquake regions (0.3–30 s).
522 Following Ide & Maury (2018), the wide range of characteristic time suggests the width variations of
523 slow earthquake source area in Hyuga-nada. The slow earthquakes in Hyuga-nada may have various
524 spectral features.

525

526 **Acknowledgements**

527 We thank Ryosuke Ando, Aitaro Kato, Satoshi Ide, Asuka Yamaguchi, Shoichi Yoshioka,
528 Takashi Tonegawa, Ryuta Arai, Masaru Nakano, Takane Hori, Eiichiro Araki, and Yojiro Yamamoto
529 for their valuable discussions. We appreciate Youichi Asano for providing the shallow VLF data in
530 2010. This research was supported by the JSPS KAKENHI Grant in Science Research on Innovative
531 Areas “Science of Slow Earthquakes” (JP16H06472), Grant-in-Aid for Scientific Research on

532 Transformative Research Areas (A) “Science of Slow-to-Fast earthquakes” (JP21H05205), and JSPS
533 Research Fellowship DC1 (JP19J20760). This study was also supported by the ERI JURP 2021-S-
534 B102. This research is part of Satoru Baba’s PhD thesis (Baba, 2022).

535

536 **Author contribution statement**

537 SB conducted analysis and drafted the manuscript. SB, ST, KO, TA, YY, and MS contributed
538 the interpretation of this study. YY and MS designed the ocean bottom seismometer observation. All
539 authors read and approved the manuscript.

540

541 **Data availability statement**

542 A part of OBS data for this study was acquired by “Research project for compound disaster
543 mitigation on the great earthquakes and tsunamis around the Nankai Trough region,” a project of the
544 Ministry of Education, Culture, Sports, Science and Technology, Japan. The OBS data is available
545 from the corresponding author upon request. We used the F-net broadband seismograms from the
546 National Research Institute for Earth and Disaster Resilience (2019) and the earthquake catalogues
547 from the Japan Meteorological Agency
548 (https://www.data.jma.go.jp/svd/eqev/data/bulletin/index_e.html). OpenSWPC code Version 5.0.2
549 (Maeda *et al.* 2017) was utilized to calculate synthetic waveforms. We used the Fujitsu PRIMERGY
550 CX600M1/CX1640M1 (Oakforest-PACS) at the Information Technology Center, the University of
551 Tokyo for numerical simulations. Generic mapping tools (Wessel *et al.* 2013) and the Seismic Analysis
552 Code (Helfrich *et al.*, 2013) are used to prepare figures and process seismograms, respectively.
553 Catalogues of shallow tremors detected by Yamashita *et al.* (2015; 2021) can be downloaded from the
554 Slow Earthquake Database (Kano, Aso, *et al.* 2018). The estimated tremor energies and VLFE
555 moments are provided in an open access repository, zenodo (<https://doi.org/10.5281/zenodo.7226845>).

556

557 **References**

- 558 Amante, C., & Eakins, B.W. 2009. ETOPO1 1 Arc-Minute Global Relief Model: Procedures, Data
559 Sources and Analysis. NOAA Technical Memorandum NESDIS NGDC-24.
560 <https://doi.org/10.7289/V5C8276M>
- 561 Ando, R., Nakata, R. & Hori, T., 2010. A slip pulse model with fault heterogeneity for low-
562 frequency earthquakes and tremor along plate interfaces. *Geophys Res Lett*, **37**, 1–5.
563 doi:10.1029/2010GL043056
- 564 Ando, R., Takeda, N. & Yamashita, T., 2012. Propagation dynamics of seismic and aseismic slip
565 governed by fault heterogeneity and Newtonian rheology. *Journal of Geophysical Research B:*
566 *Solid Earth*, **117**, Blackwell Publishing Ltd. doi:10.1029/2012JB009532
- 567 Aoi, S., Asano, Y., Kunugi, T., Kimura, T., Uehira, K., Takahashi, N., Ueda, H., *et al.*, 2020.

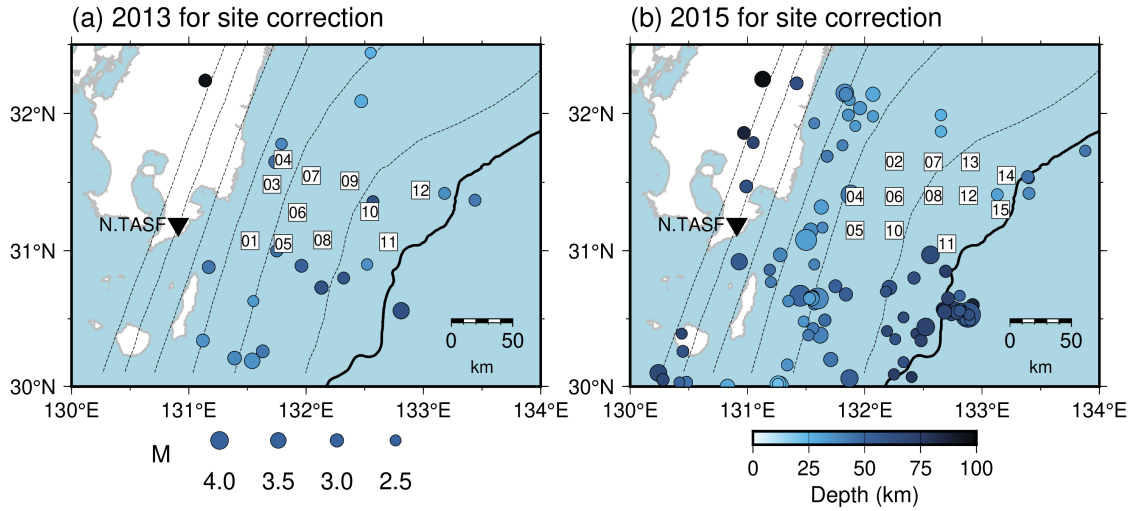
- 568 MOWLAS: NIED observation network for earthquake, tsunami and volcano. *Earth, Planets and*
569 *Space*, **72**, Springer Berlin Heidelberg. doi:10.1186/s40623-020-01250-x
- 570 Asano, Y., Obara, K., Matsuzawa, T., Hirose, H. & Ito, Y., 2015. Possible shallow slow slip events in
571 Hyuga-nada, Nankai subduction zone, inferred from migration of very low frequency
572 earthquakes. *Geophys Res Lett*, **42**, 331–338. doi:10.1002/2014GL062165
- 573 Baba, S., 2022. Spatiotemporal characteristics of slow earthquakes in subduction zones around Japan.
574 PhD thesis of the University of Tokyo, Japan.
- 575 Baba, S., Obara, K., Takemura, S., Takeo, A. & Abers, G.A., 2021. Shallow Slow Earthquake Episodes
576 Near the Trench Axis Off Costa Rica. *J Geophys Res Solid Earth*. doi:10.1029/2021JB021706
- 577 Baba, S., Takemura, S., Obara, K. & Noda, A., 2020. Slow Earthquakes Illuminating Interplate
578 Coupling Heterogeneities in Subduction Zones. *Geophys Res Lett*, **47**, 4–5.
579 doi:10.1029/2020GL088089
- 580 Bartlow, N.M., Miyazaki, S., Bradley, A.M. & Segall, P., 2011. Space-time correlation of slip and
581 tremor during the 2009 Cascadia slow slip event. *Geophys Res Lett*, **38**, Blackwell Publishing
582 Ltd. doi:10.1029/2011GL048714
- 583 Chesley, C., Naif, S., Key, K. & Bassett, D., 2021. Fluid-rich subducting topography generates
584 anomalous forearc porosity. *Nature*, **595**, 255–260, Nature Research. doi:10.1038/s41586-021-
585 03619-8
- 586 DeMets, C., Gordon, R.G., Argus, D.F. & Stein, S., 1994. Effect of recent revisions to the geomagnetic
587 reversal time scale on estimates of current plate motions. *Geophys Res Lett*, **21**, 2191–2194.
588 doi:10.1029/94GL02118
- 589 Dragert, H., Wang, K., James, T.S., 2001. A Silent Slip Event on the Deeper Cascadia Subduction
590 Interface. *Science (1979)*, **292**, 1525–1528. doi:10.1126/science.1060152
- 591 Helffrich, G., Wookey, J., & Bastow, I. (2013). The Seismic Analysis Code. Cambridge: Cambridge
592 University Press. <https://doi.org/10.1017/CBO9781139547260>
- 593 Hirose, H., Hirahara, K., Kimata, F., Fujii, N. & Miyazaki, S., 1999. A slow thrust slip event following
594 the two 1996 Hyuganada earthquakes beneath the Bungo Channel, southwest Japan. *Geophys*
595 *Res Lett*, **26**, 3237–3240. doi:10.1029/1999GL010999
- 596 Houston, H., Delbridge, B.G., Wech, A.G., & Creager, K.C. 2011. Rapid tremor reversals in Cascadia
597 generated by a weakened plate interface. *Nature Geoscience*, **4**, 404-409,
598 doi:10.1038/NGE01157
- 599 Ide, S., 2016. Characteristics of slow earthquakes in the very low frequency band: Application to the
600 Cascadia subduction zone. *J Geophys Res Solid Earth*, **121**, 5942–5952.
601 doi:10.1002/2016JB013085
- 602 Ide, S., Beroza, G.C., Shelly, D.R. & Uchide, T., 2007. A scaling law for slow earthquakes. *Nature*,
603 **447**, 76–79. doi:10.1038/nature05780

- 604 Ide, S., Imanishi, K., Yoshida, Y., Beroza, G.C. & Shelly, D.R., 2008. Bridging the gap between
605 seismically and geodetically detected slow earthquakes. *Geophys Res Lett*, **35**, 2–7.
606 doi:10.1029/2008GL034014
- 607 Ide, S. & Maury, J., 2018. Seismic Moment, Seismic Energy, and Source Duration of Slow
608 Earthquakes: Application of Brownian slow earthquake model to three major subduction zones.
609 *Geophys Res Lett*, **45**, 3059–3067. doi:10.1002/2018GL077461
- 610 Ide, S. & Yabe, S., 2014. Universality of slow earthquakes in the very low frequency band. *Geophys*
611 *Res Lett*, **41**, 2786–2793. doi:10.1002/2014GL059712
- 612 Igarashi, T., 2020. Catalog of small repeating earthquakes for the Japanese Islands. *Earth, Planets and*
613 *Space*, **72**, Springer Berlin Heidelberg. doi:10.1186/s40623-020-01205-2
- 614 Ito, Y., Obara, K., Shiomi, K., Sekine, S. & Hirose, H., 2007. Slow Earthquakes Coincident with
615 Episodic Tremors and Slow Slip Events. *Science (1979)*, **315**, 503–506.
616 doi:10.1126/science.1134454
- 617 Kanamori, H. & Anderson, D.L., 1975. THEORETICAL BASIS OF SOME EMPIRICAL
618 RELATIONS IN SEISMOLOGY. *Bulletin of the Seismological Society of America*, Vol. 65.
619 Retrieved from [http://pubs.geoscienceworld.org/ssa/bssa/article-](http://pubs.geoscienceworld.org/ssa/bssa/article-pdf/65/5/1073/5320189/bssa0650051073.pdf)
620 [pdf/65/5/1073/5320189/bssa0650051073.pdf](http://pubs.geoscienceworld.org/ssa/bssa/article-pdf/65/5/1073/5320189/bssa0650051073.pdf)
- 621 Kanamori, H. & Rivera, L., 2006. Energy partitioning during an earthquake. *Geophysical Monograph*
622 *Series*, **170**, 3–13. doi:10.1029/170GM03
- 623 Kaneko, L., Ide, S. & Nakano, M., 2018. Slow Earthquakes in the Microseism Frequency Band (0.1–
624 1.0 Hz) off Kii Peninsula, Japan. *Geophys Res Lett*, **45**, 2618–2624. doi:10.1002/2017GL076773
- 625 Kano, M., Aso, N., Matsuzawa, T., Ide, S., Annoura, S., Arai, R., Baba, S., *et al.*, 2018a. Development
626 of a Slow Earthquake Database. *Seismological Research Letters*, **89**, 1566–1575.
627 doi:10.1785/0220180021
- 628 Kano, M., Kato, A., Ando, R. & Obara, K., 2018b. Strength of tremor patches along deep transition
629 zone of a megathrust. *Sci Rep*, **8**, Nature Publishing Group. doi:10.1038/s41598-018-22048-8
- 630 Kato, A., Obara, K., Igarashi, T., Tsuruoka, H., Nakagawa, S. & Hirata, N., 2012. Propagation of Slow
631 Slip Leading Up to the 2011 Mw 9.0 Tohoku-Oki Earthquake. *Science (1979)*, **335**, 705–708.
632 doi:10.1126/science.1215141
- 633 Koketsu, K., Miyake, H., Suzuki, H., 2012. Japan Integrated Velocity Structure Model Version 1. In:
634 Proceedings of the 15th World Conference on Earthquake Engineering, Lisbon, Portugal, 24-28
635 September, Paper 1773.
- 636 Maeda, T., Takemura, S. & Furumura, T., 2017. OpenSWPC: An open-source integrated parallel
637 simulation code for modeling seismic wave propagation in 3D heterogeneous viscoelastic media
638 4. Seismology. *Earth, Planets and Space*, **69**, Springer Berlin Heidelberg. doi:10.1186/s40623-
639 017-0687-2

- 640 Masuda, K., Ide, S., Ohta, K. & Matsuzawa, T., 2020. Bridging the gap between low-frequency and
641 very-low-frequency earthquakes. *Earth, Planets and Space*, **72**, Springer Berlin Heidelberg.
642 doi:10.1186/s40623-020-01172-8
- 643 Nadeau, R.M. & McEvilly, T. v, 1999. Fault Slip Rates at Depth from Recurrence Intervals of
644 Repeating Microearthquakes. *A. A. Koulakov and B. I. Shklovskii Phys. Rev. B*, Vol. 27.
- 645 Nakanishi, A., Takahashi, N., Yamamoto, Y., Takahashi, T., Citak, S.O., Nakamura, T., Obana, K., *et*
646 *al.*, 2018. Three-dimensional plate geometry and P-wave velocity models of the subduction zone
647 in SW Japan: Implications for seismogenesis. *Special Paper of the Geological Society of*
648 *America*, **534**, 69–86, Geological Society of America. doi:10.1130/2018.2534(04)
- 649 Nakata, R., Ando, R., Hori, T. & Ide, S., 2011. Generation mechanism of slow earthquakes: Numerical
650 analysis based on a dynamic model with brittle-ductile mixed fault heterogeneity. *J Geophys Res*
651 *Solid Earth*, **116**, Blackwell Publishing Ltd. doi:10.1029/2010JB008188
- 652 National Research Institute for Earth Science and Disaster Resilience, 2019. NIED F-net.
653 <https://doi.org/10.17598/NIED.0005>
- 654 Obara, K., 2002. Nonvolcanic Deep Tremor Associated with Subduction in Southwest Japan. *Science*
655 (1979), **296**, 1679–1681. doi:10.1126/science.1070378
- 656 Obara, K. & Ito, Y., 2005. Very low frequency earthquakes excited by the 2004 off Kii peninsula
657 earthquakes: A dynamic deformation process in the large accretionary prism. *Earth, Planets and*
658 *Space*, **57**, 321–326. doi:10.1186/BF03352570
- 659 Obara, K. & Kato, A., 2016. Connecting slow earthquakes to huge earthquakes. *Science*, **353**, 253–
660 257. doi:10.1126/science.aaf1512
- 661 Ohta, K. & Ide, S., 2017. Resolving the Detailed Spatiotemporal Slip Evolution of Deep Tremor in
662 Western Japan. *J Geophys Res Solid Earth*, **122**, 10,009-10,036. doi:10.1002/2017JB014494
- 663 Rogers, G. & Dragert, H., 2003. Episodic Tremor and Slip on the Cascadia Subduction Zone: The
664 Chatter of Silent Slip. *Science (1979)*, **300**, 1942–1943. doi:10.1126/science.1084783
- 665 Shelly, D.R., Beroza, G.C., Ide, S. & Nakamura, S., 2006. Low-frequency earthquakes in Shikoku,
666 Japan, and their relationship to episodic tremor and slip. *Nature*, **442**, 188–191.
667 doi:10.1038/nature04931
- 668 Takemura, S., Baba, S., Yabe, S., Emoto, K., Shiomi, K. & Matsuzawa, T., 2022a. Source
669 Characteristics and Along-Strike Variations of Shallow Very Low Frequency Earthquake
670 Swarms on the Nankai Trough Shallow Plate Boundary. *Geophys Res Lett*, **49**, John Wiley and
671 Sons Inc. doi:10.1029/2022GL097979
- 672 Takemura, S., Matsuzawa, T., Noda, A., Tonegawa, T., Asano, Y., Kimura, T. & Shiomi, K., 2019.
673 Structural Characteristics of the Nankai Trough Shallow Plate Boundary Inferred From Shallow
674 Very Low Frequency Earthquakes. *Geophys Res Lett*, **46**, 4192–4201.
675 doi:10.1029/2019GL082448

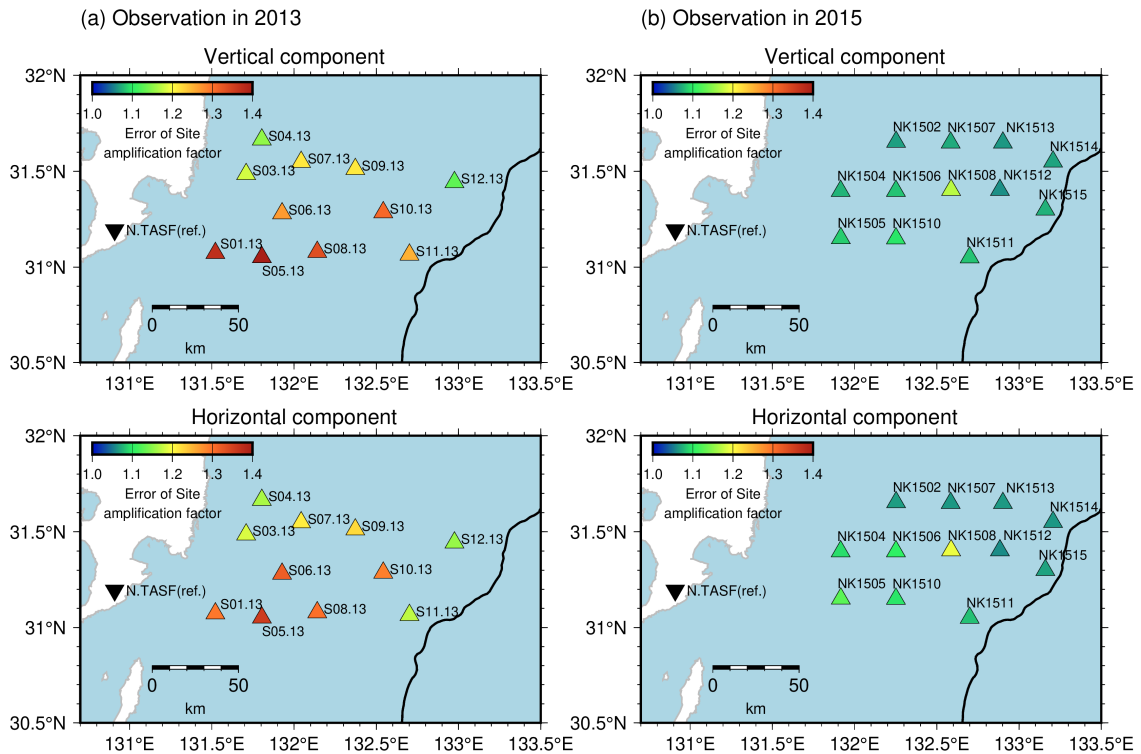
- 676 Takemura, S., Obara, K., Shiomi, K. & Baba, S., 2022b. Spatiotemporal Variations of Shallow Very
677 Low Frequency Earthquake Activity Southeast Off the Kii Peninsula, Along the Nankai Trough,
678 Japan. *J Geophys Res Solid Earth*, **127**, John Wiley and Sons Inc. doi:10.1029/2021JB023073
- 679 Takemura, S., Okuwaki, R., Kubota, T., Shiomi, K., Kimura, T. & Noda, A., 2020. Centroid moment
680 tensor inversions of offshore earthquakes using a three-dimensional velocity structure model:
681 slip distributions on the plate boundary along the Nankai Trough. *Geophys J Int*, **222**, 1109–
682 1125, Oxford University Press. doi:10.1093/gji/ggaa238
- 683 Tonegawa, T., Yamashita, Y., Takahashi, T., Shinohara, M., Ishihara, Y., Kodaira, S. & Kaneda, Y.,
684 2020. Spatial relationship between shallow very low frequency earthquakes and the subducted
685 Kyushu-Palau Ridge in the Hyuga-nada region of the Nankai subduction zone. *Geophys J Int*,
686 1542–1554, Oxford University Press. doi:10.1093/gji/ggaa264
- 687 Uchida, N. & Matsuzawa, T., 2011. Coupling coefficient, hierarchical structure, and earthquake cycle
688 for the source area of the 2011 off the Pacific coast of Tohoku earthquake inferred from small
689 repeating earthquake data. *Earth, Planets and Space*, **63**, 675–679, Springer Berlin.
690 doi:10.5047/eps.2011.07.006
- 691 Uchida, N., Matsuzawa, T., Hasegawa, A. & Igarashi, T., 2003. Interplate quasi-static slip off Sanriku,
692 NE Japan, estimated from repeating earthquakes. *Geophys Res Lett*, **30**, American Geophysical
693 Union. doi:10.1029/2003GL017452
- 694 Vaca, S., Vallée, M., Nocquet, J.M., Battaglia, J. & Régnier, M., 2018. Recurrent slow slip events as a
695 barrier to the northward rupture propagation of the 2016 Pedernales earthquake (Central
696 Ecuador). *Tectonophysics*, **724–725**, 80–92, Elsevier. doi:10.1016/j.tecto.2017.12.012
- 697 Wang, K. & Bilek, S.L., 2011. Do subducting seamounts generate or stop large earthquakes? *Geology*,
698 **39**, 819–822, Geological Society of America. doi:10.1130/G31856.1
- 699 Wessel, P., Smith, W.H.F., Scharroo, R., Luis, J. & Wobbe, F., 2013. Generic mapping tools: Improved
700 version released. *Eos (Washington DC)*, **94**, 409–410. doi:10.1002/2013EO450001
- 701 Yabe, S., Baba, S., Tonegawa, T., Nakano, M. & Takemura, S., 2021. Seismic energy radiation and
702 along-strike heterogeneities of shallow tectonic tremors at the Nankai Trough and Japan Trench.
703 *Tectonophysics*, 228714, Elsevier B.V. doi:10.1016/j.tecto.2020.228714
- 704 Yabe, S., Tonegawa, T. & Nakano, M., 2019. Scaled Energy Estimation for Shallow Slow Earthquakes.
705 *J Geophys Res Solid Earth*, **124**, 1507–1519. doi:10.1029/2018JB016815
- 706 Yamamoto, Y., Ariyoshi, K., Yada, S., Nakano, M. & Hori, T., 2022. Spatio-temporal distribution of
707 shallow very-low-frequency earthquakes between December 2020 and January 2021 in
708 Kumano-nada, Nankai subduction zone, detected by a permanent seafloor seismic network.
709 *Earth, Planets and Space*, **74**, 14. doi:10.1186/s40623-022-01573-x
- 710 Yamamoto, Y., Obana, K., Takahashi, T., Nakanishi, A., Kodaira, S. & Kaneda, Y., 2013. Imaging of
711 the subducted kyushu-palau ridge in the hyuga-nada region, western nankai trough subduction

- 712 zone. *Tectonophysics*, **589**, 90–102. doi:10.1016/j.tecto.2012.12.028
- 713 Yamashita, Y, Asano, Y., Shimizu, H., Uchida, K., Hirano, S., Umakoshi, K., Miyamachi, H., *et al.*,
- 714 2015. Migrating tremor off southern Kyushu as evidence for slow slip of a shallow subduction
- 715 interface. *Science (1979)*, **348**, 676–679. doi:10.1126/science.aaa4242
- 716 Yamashita, Y., Shimizu, H. & Goto, K., 2012. Small repeating earthquake activity, interplate quasi-
- 717 static slip, and interplate coupling in the Hyuga-nada, southwestern Japan subduction zone.
- 718 *Geophys Res Lett*, **39**, Blackwell Publishing Ltd. doi:10.1029/2012GL051476
- 719 Yamashita, Y., Shinohara, M. & Yamada, T., 2021. Shallow tectonic tremor activities in Hyuga-nada,
- 720 Nankai subduction zone, based on long-term broadband ocean bottom seismic observations.
- 721 *Earth, Planets and Space*, **73**, 196. doi:10.1186/s40623-021-01533-x
- 722
- 723



724
725
726
727
728
729

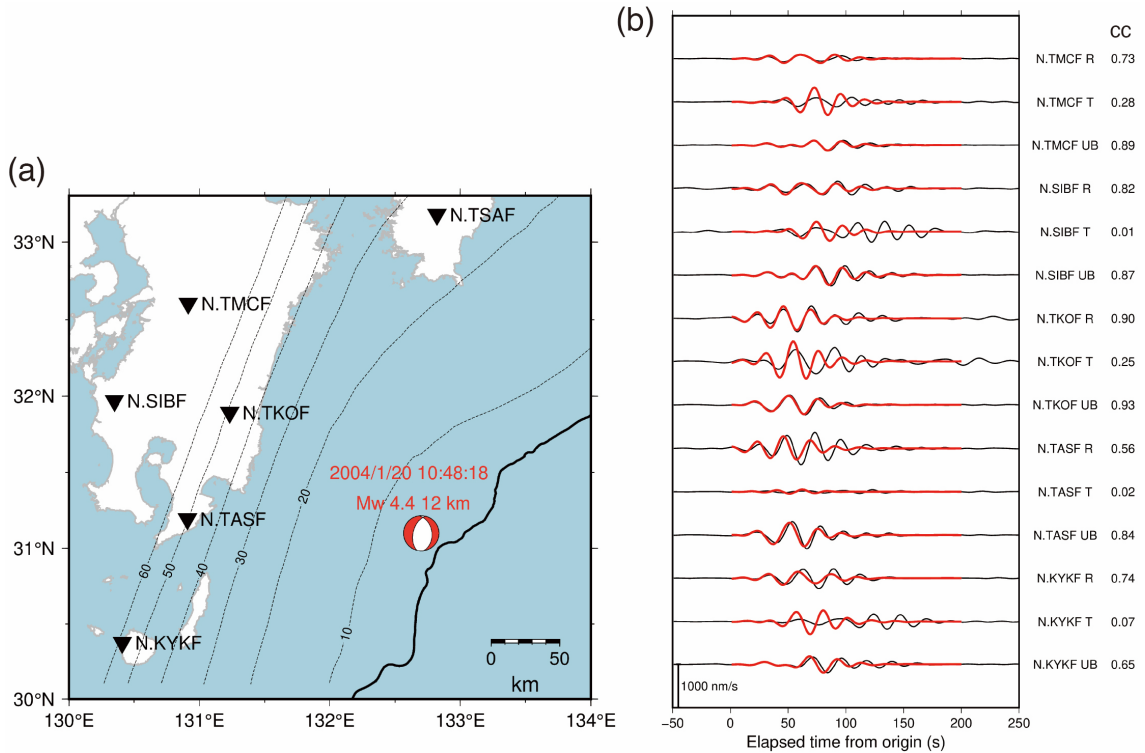
Figure S1. Distribution of earthquakes used for the estimation of the site amplification factors. Inverted triangles display the locations of the F-net stations. Squares represents the locations of OBSs. Black line and dotted contours are the same as displayed in Fig. 6.



730
731
732
733
734

Figure S2. Estimation errors of site amplification factors at each station. Inverted triangle indicates the location of the F-net station, N.TASF. Black line is the same as displayed in Fig. 3.

735

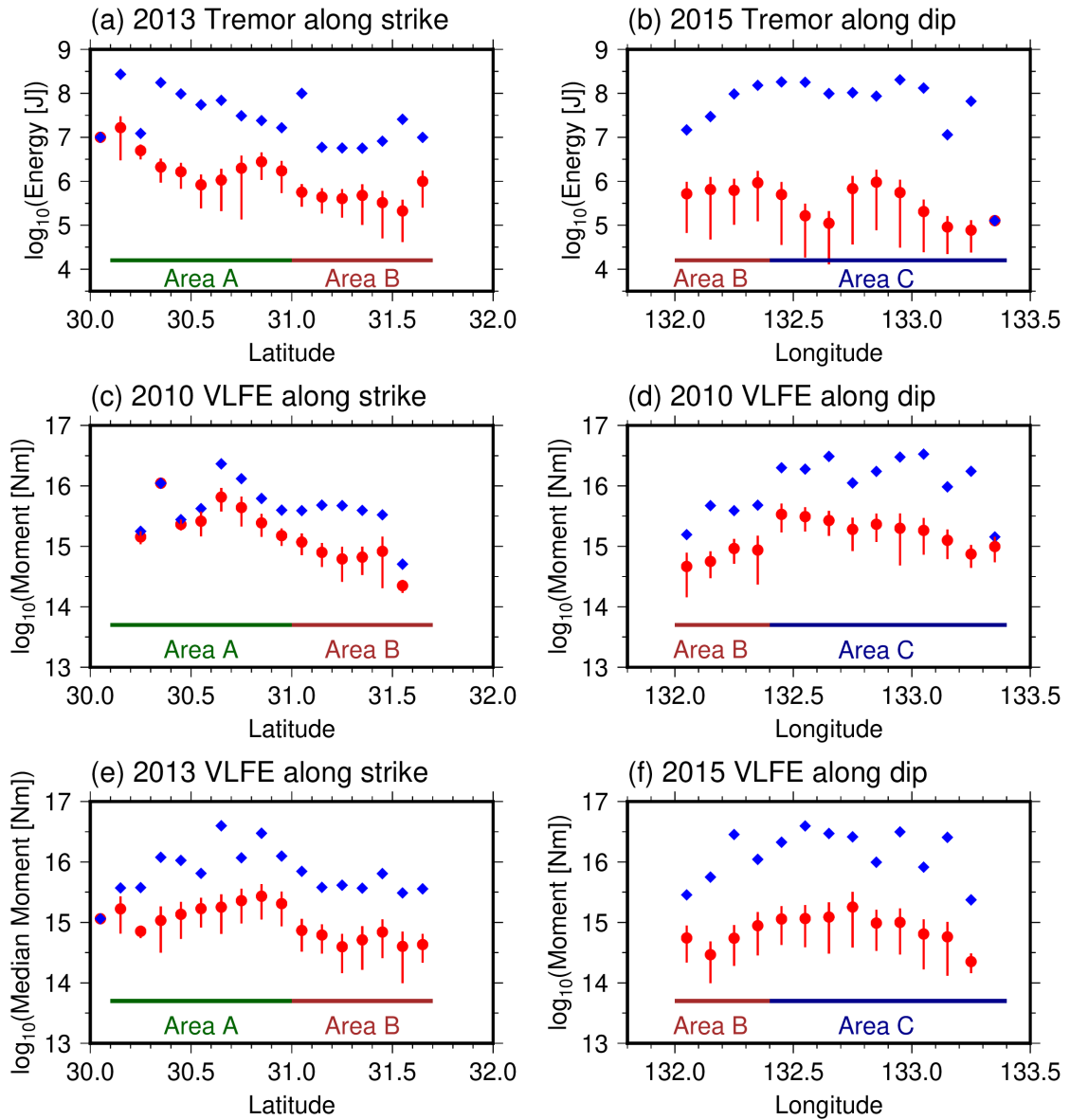


736

737

738 **Figure S3.** Simulated waveforms of a regular earthquake that occurred in northern Hyuga-nada. (a)
 739 Focal mechanism of the regular earthquake listed in the catalog by Takemura et al. (2020; catalog:
 740 doi:10.5281/zenodo.3821172). Black line, inverted triangles, and dotted contours are the same as
 741 displayed in Fig. 6. (b) Observed (black lines) and simulated (red lines) waveforms of the earthquake
 742 at each F-net station. The assumed source time function was a Küpper wavelet with a source duration
 743 of 1 s. Black and red lines are the observed and the simulated waveforms, respectively. The simulation
 744 setting is the same as described in Section 2.2. R, T, and UB components represent the radial,
 745 transverse, and vertical components, respectively.

746



747

748

749 **Figure S4.** Variation in maximum and median of tremor energies and VLFE moments along strike and

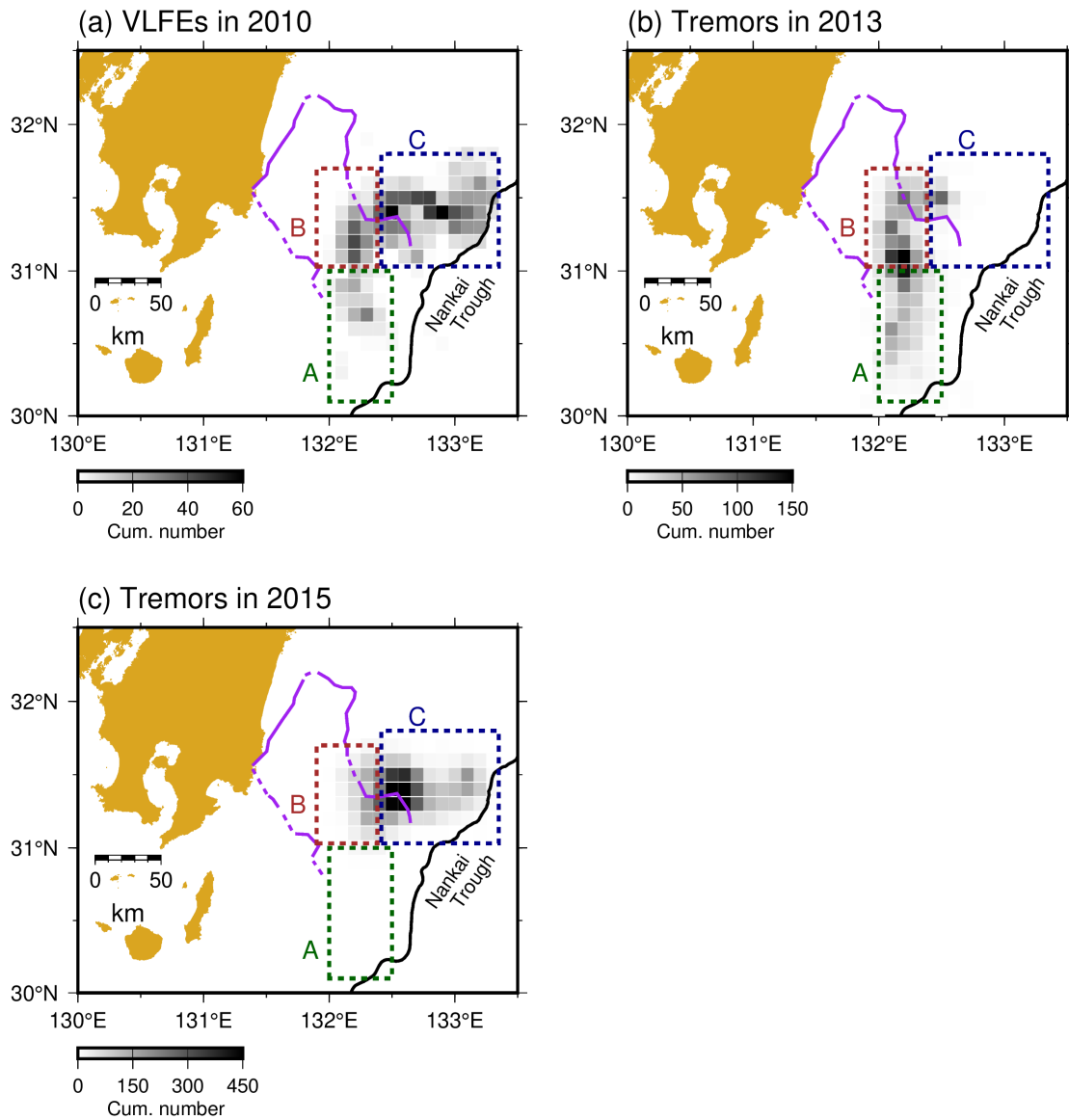
750 dip directions at 0.1° interval. Blue diamonds and red circles represent the maximum and median

751 values, respectively. Red bars show the median absolute deviation of tremor energies and VLFE

752

moments.

753



754

755

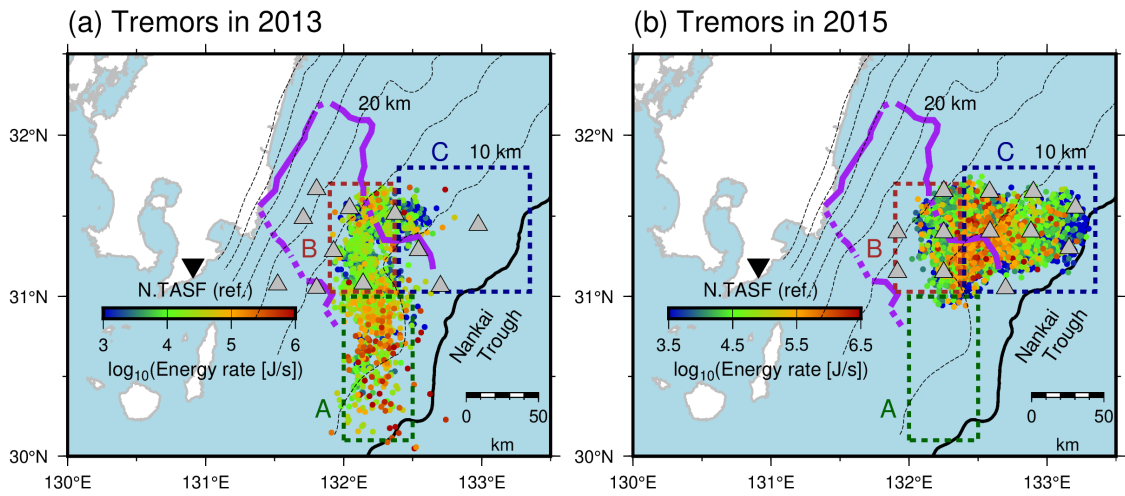
756 **Figure S5.** Event number distribution in the grid of $1^\circ \times 1^\circ$. (a), VLFs located by Asano et al. (2015),

757 (b), tremors located by Yamashita et al. (2015), (c), tremors located by Yamashita et al. (2021). Colored

758 dotted rectangles, purple lines, and black lines are the same as in Fig. 7.

759

760



761

762

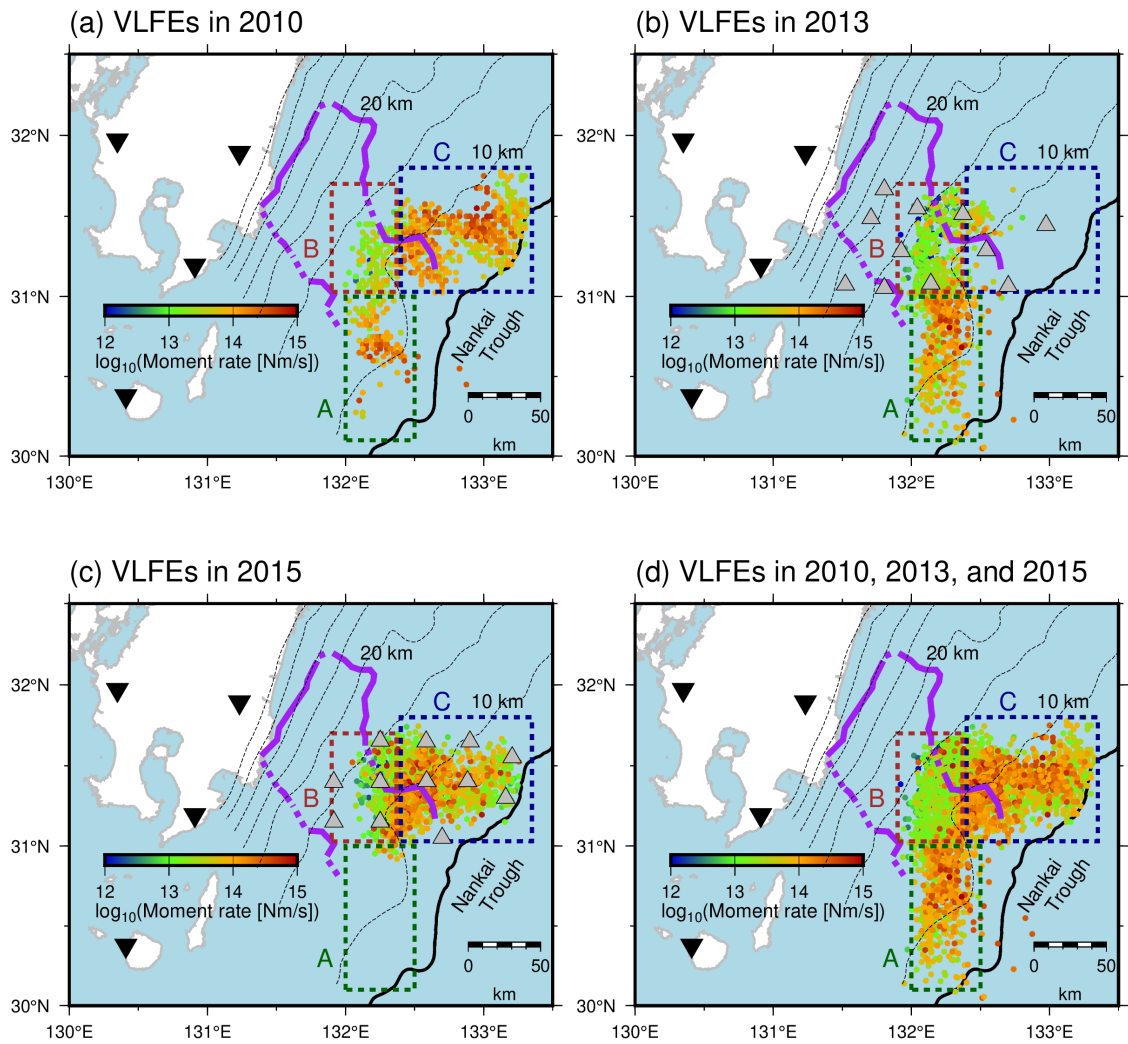
763

764

765

766

Figure S6. Spatial distribution of energy rates of shallow tremors in (a) 2013 and (c) in 2015. Colored dotted rectangles, dashed contours, purple lines, black line and gray triangles are the same as displayed in Fig. 7.



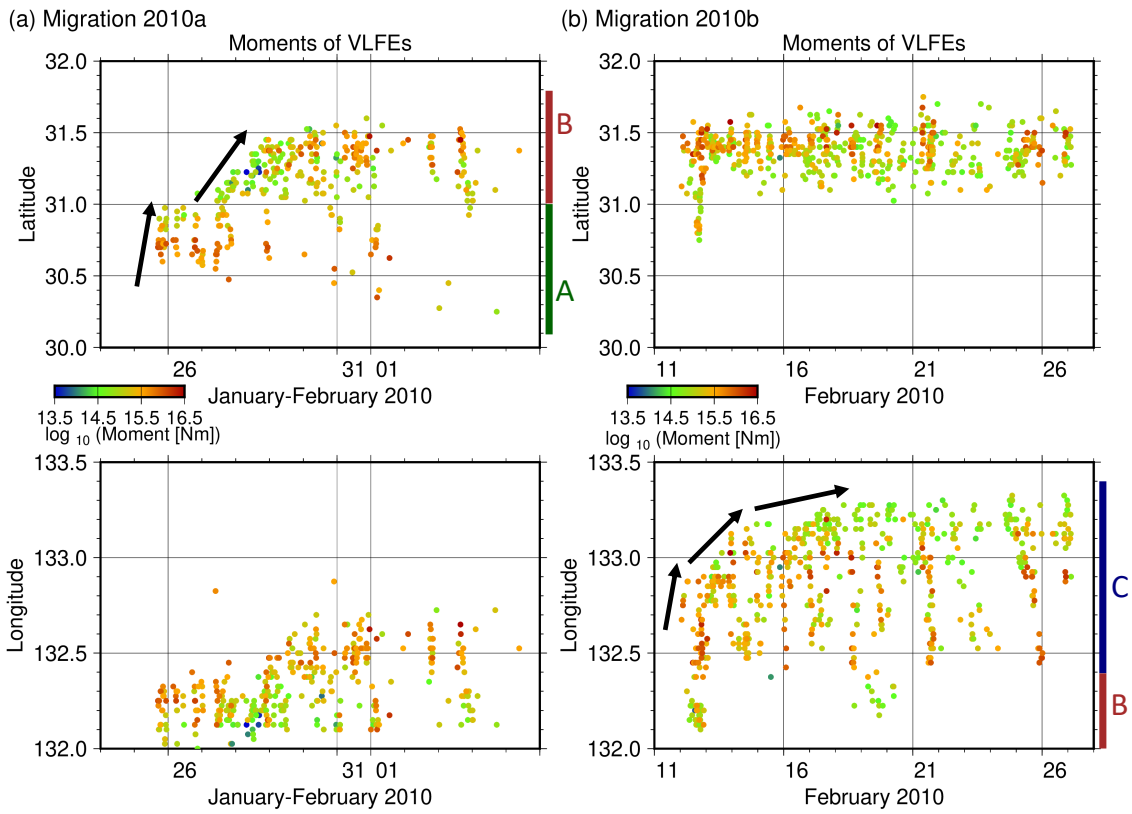
767

768

769 **Figure S7.** Spatial distribution of moment rates of shallow VLFs in (a) 2010, (b) 2013, (c) 2015,
770 and (d) all analysis periods. Colored dotted rectangles, dashed contours, purple lines, black line and
771 gray triangles are the same as displayed in Fig. 7.

772

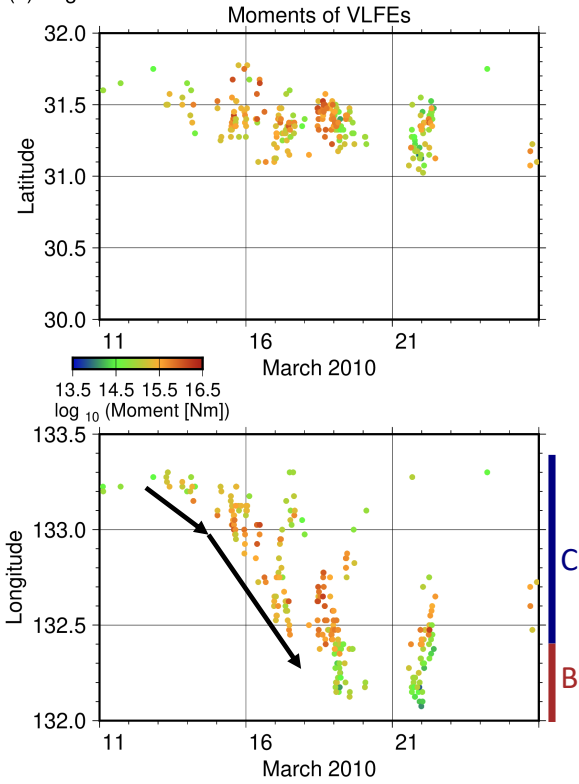
773



774

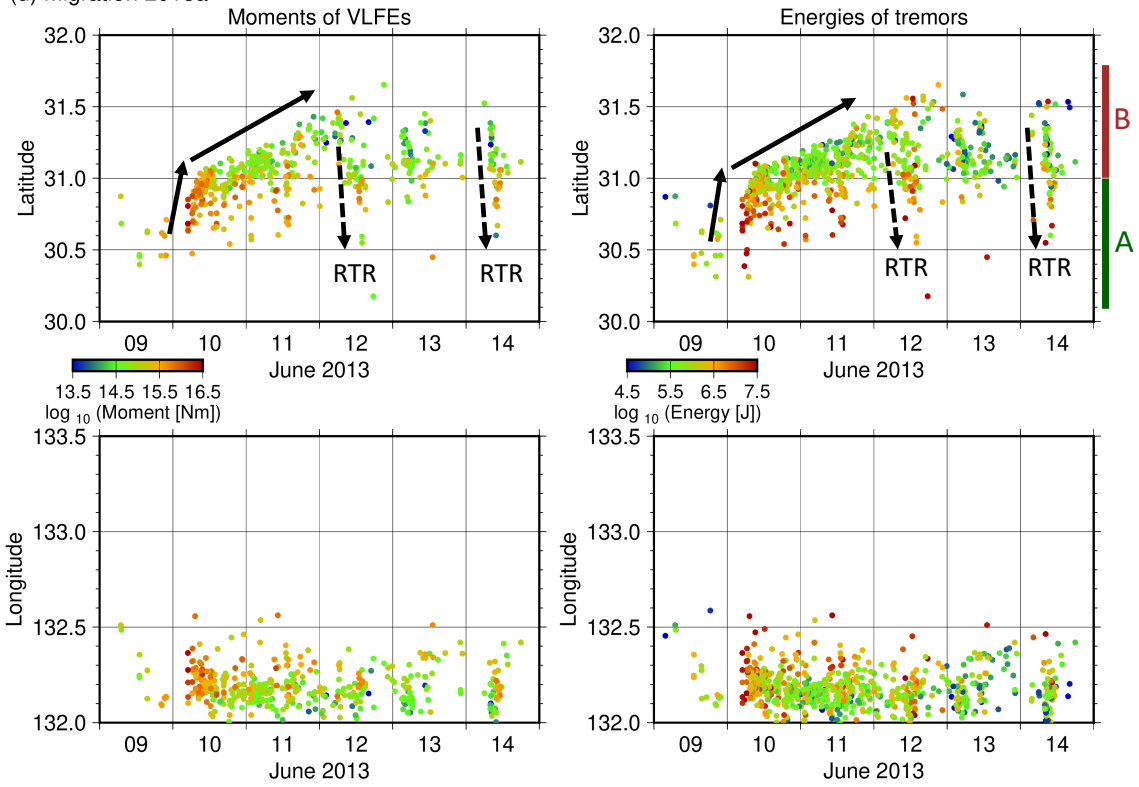
775

(c) Migration 2010c



776

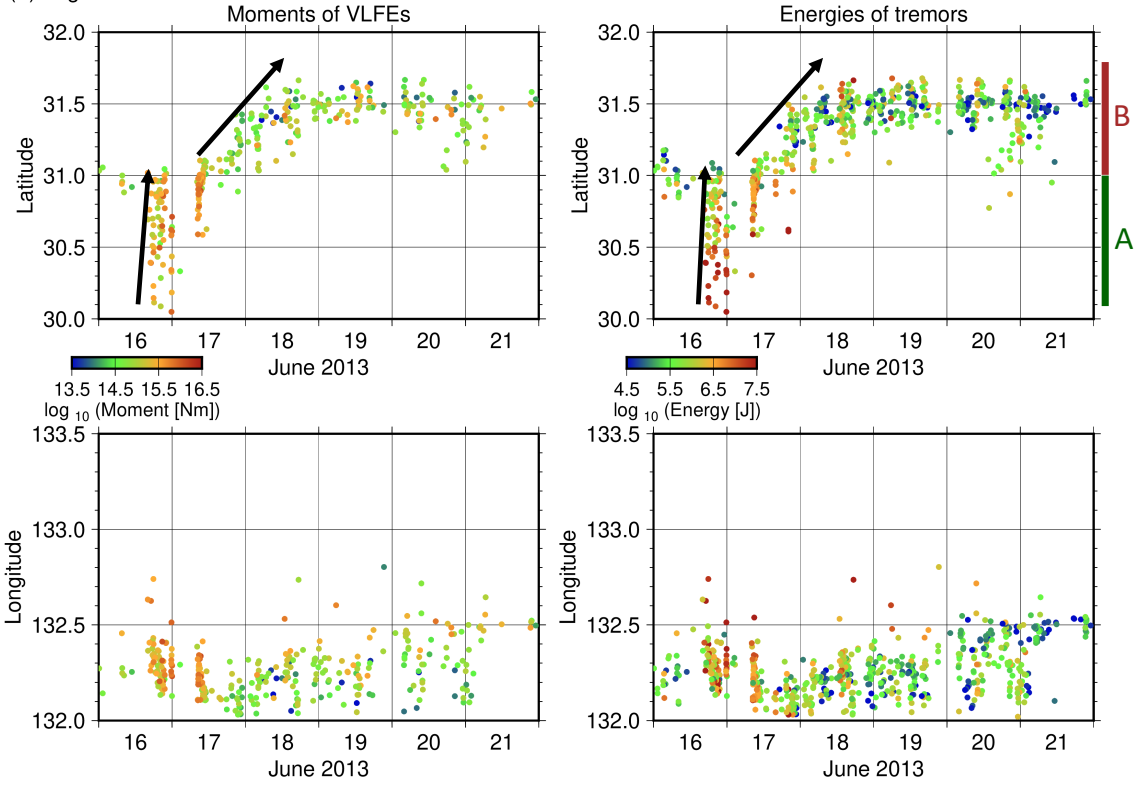
(d) Migration 2013a



777

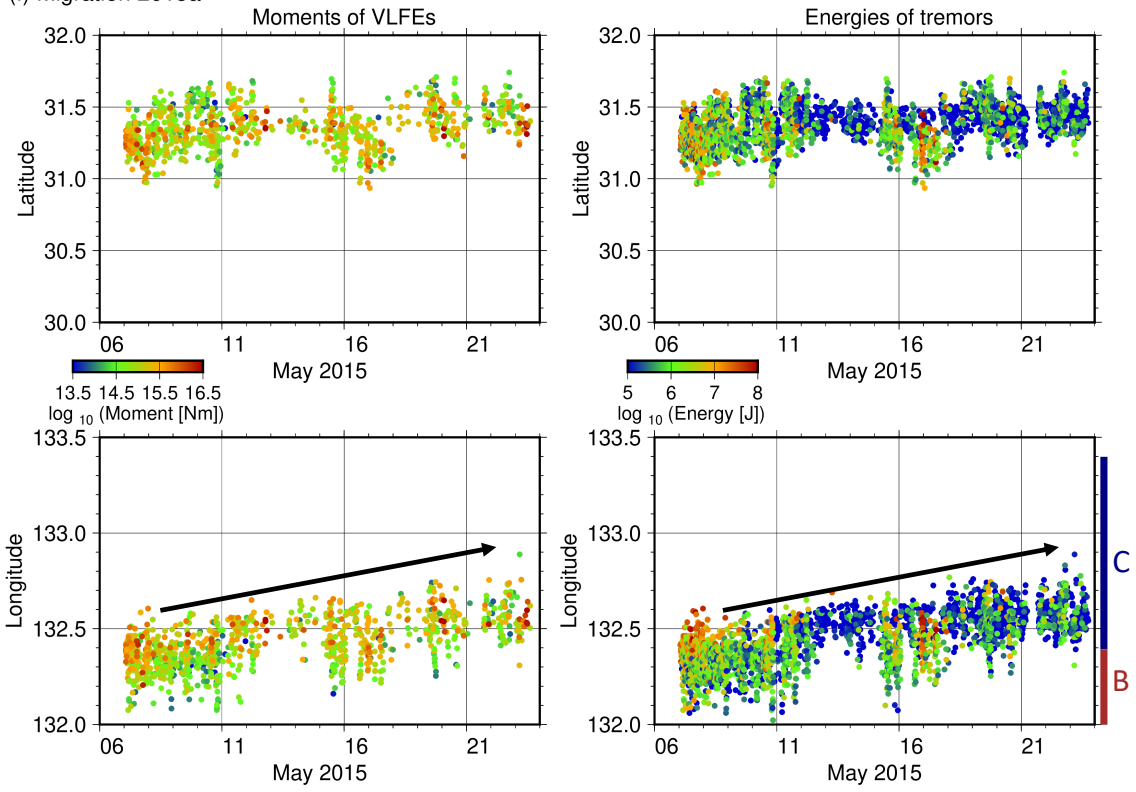
778

(e) Migration 2013b



779

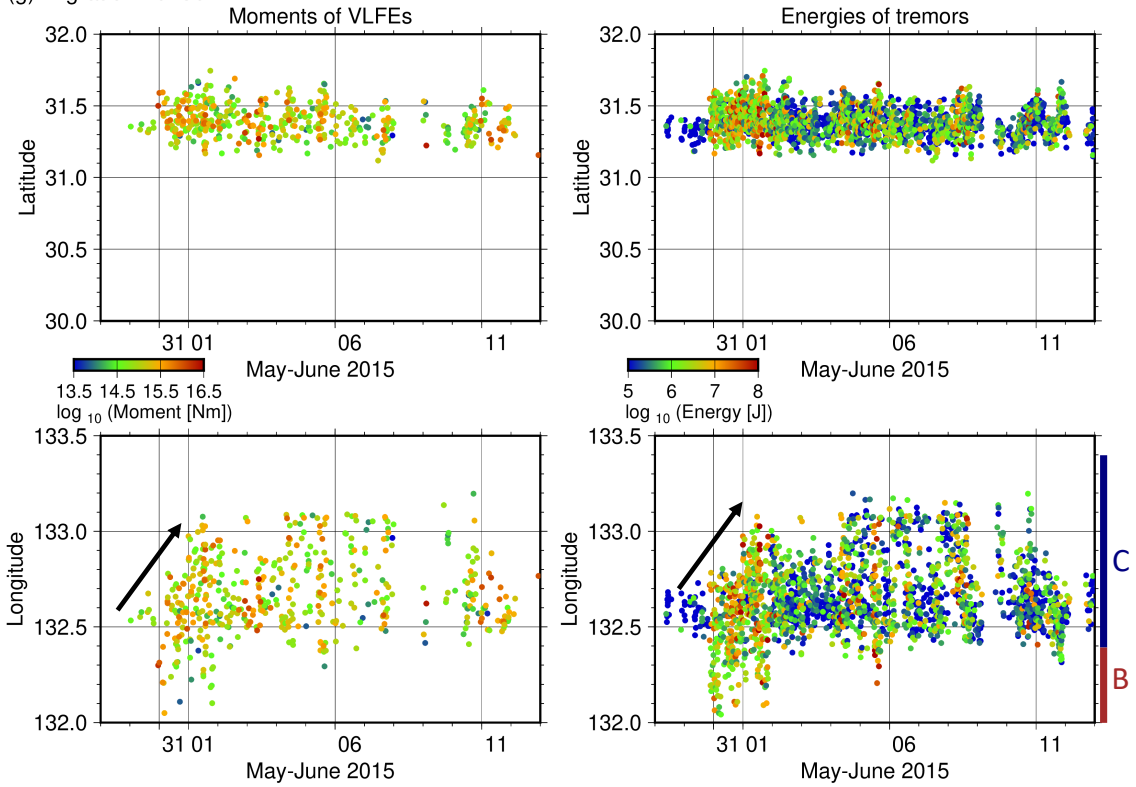
(f) Migration 2015a



780

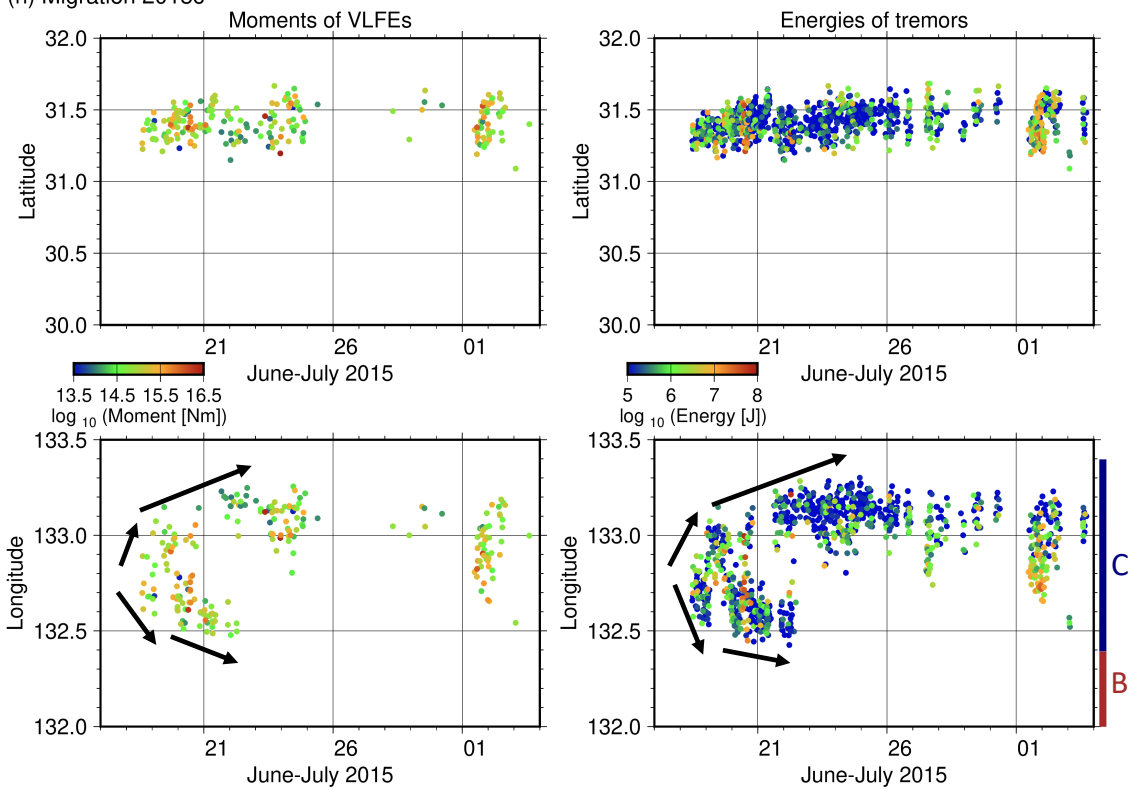
781

(g) Migration 2015b



782

(h) Migration 2015c

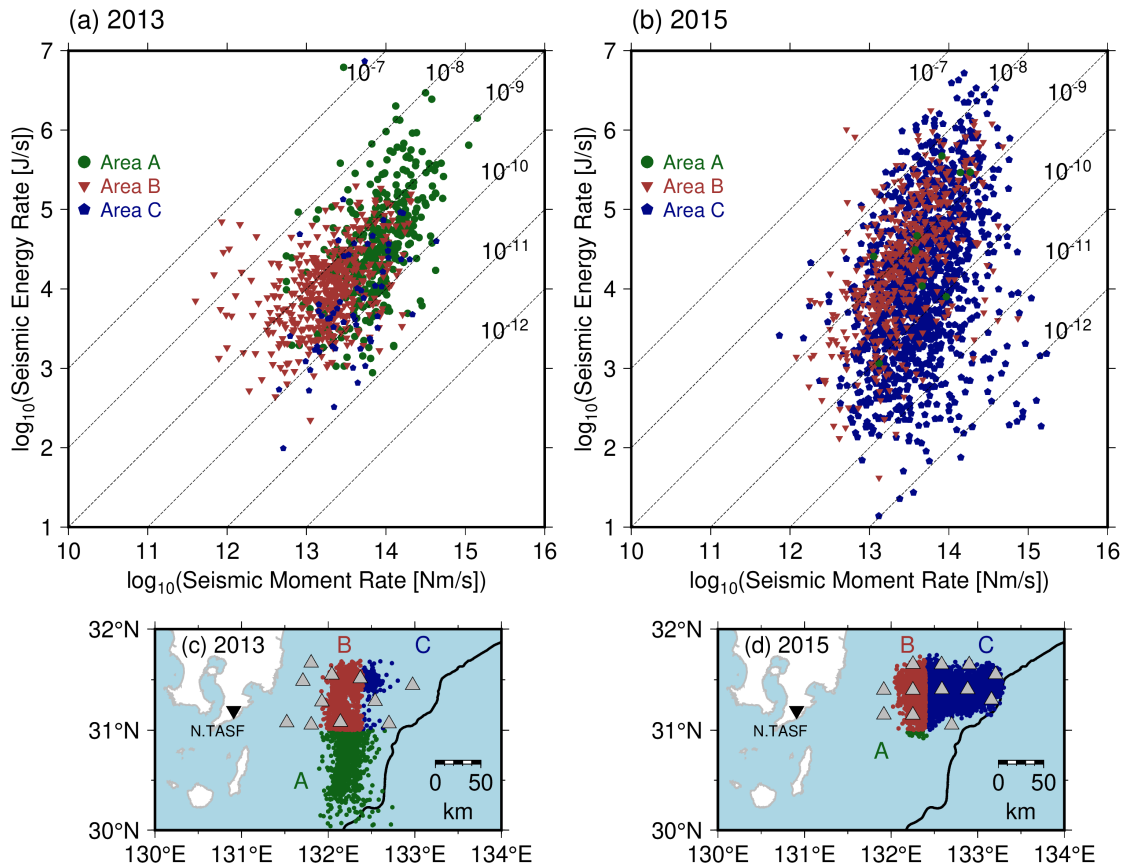


783

784

785 **Figure S8.** Spatiotemporal distributions of moments of VLFEs and energies of tremors in the
 786 directions along the N-S and E-W sections for each migration. Black arrows indicate the direction of
 787 migrations. Black dotted arrows in Fig. S8d represents the RTR.

788



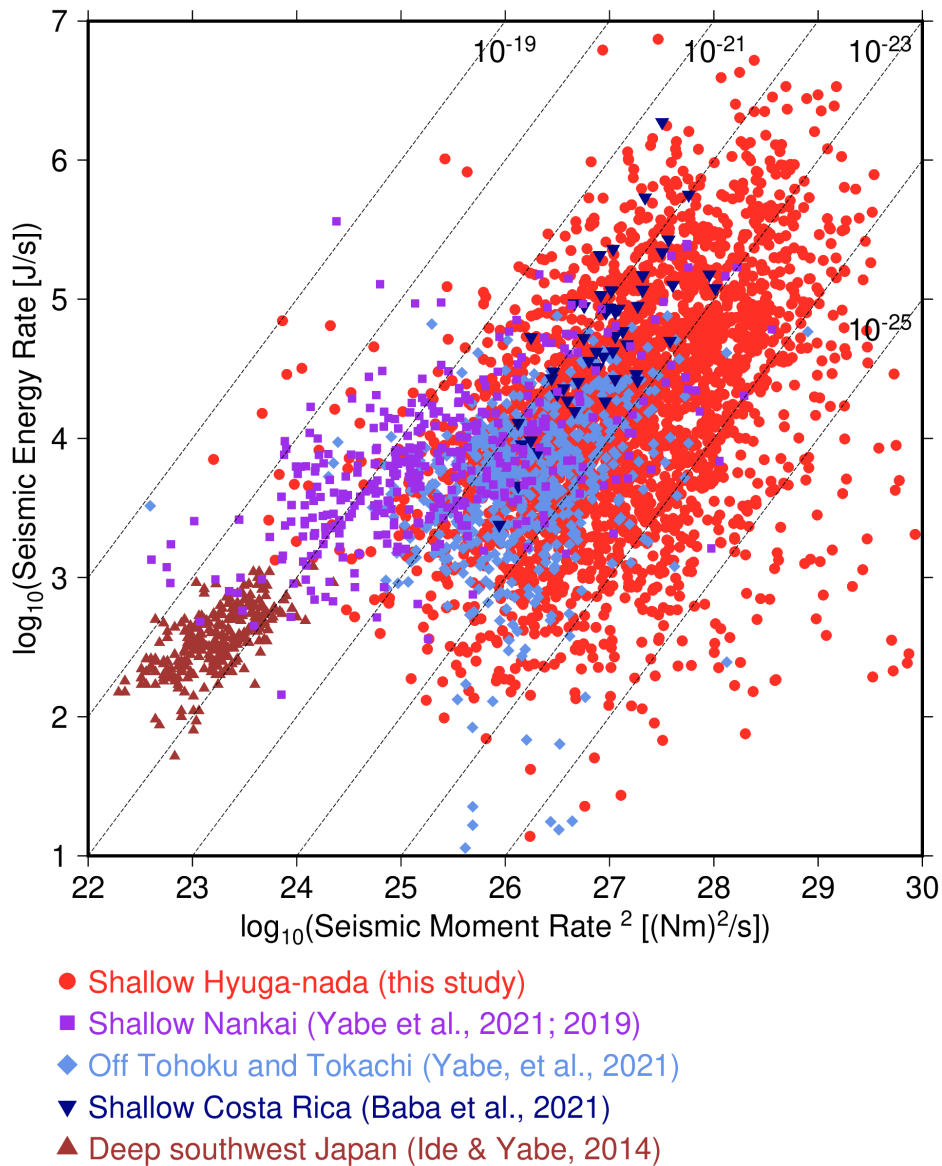
789

790

791 **Figure S9.** Relationship between seismic moment rates of VLFEs and seismic moment rates of
 792 shallow tremors at each area in Hyuga-nada (a) in 2013 and (b) in 2015. Epicenters of shallow tremors
 793 at each area (c) in 2013 and (d) in 2015. Shallow tremors in Area A, B, and C are depicted by green,
 794 brown, and dark blue dots, respectively. Black lines, gray and black inverted triangles are the same as
 795 displayed in Fig.7.

796

797



798

799

800 **Figure S10.** Relationship between seismic moment rates of VLFEs and squared seismic moment rates
801 of tremors. Red circles, purple squares, green diamonds, dark blue inverted triangles, and dark blue
802 triangles indicate the relationships between seismic moment rates of VLFEs and seismic moment rates
803 of tremors in shallow Hyuga-nada (this study), shallow Nankai except Hyuga-nada (Yabe et al. 2021,
804 2019), off Tohoku and Tokachi (Yabe et al. 2021), shallow Costa Rica (Baba et al. 2021), and deep
805 slow earthquakes (Ide, 2016; Ide and Maury, 2018; Ide and Yabe, 2014).

806

807 **Table S1.** Characteristics of migrations in Hyuga-nada.

808

	Migration direction	
2010a	Along-strike	South to north
2010b	Along-dip	Downdip to updip
2010c	Along-dip	Updip to downdip
2013a	Along-strike	South to north
2013b	Along-strike	South to north
2015a	Along-dip	Downdip to updip
2015b	Along-dip	Downdip to updip
2015c	Along-dip	Bilateral

809